Geochemistry Geophysics Geosystems G3
AN ELECTRONIC JOURNAL OF THE EARTH SCIENCES
Published by AGU and the Geochemical Society

Article
Volume 10, Number 6
10 June 2009
Q06004, doi:10.1029/2008GC002290
ISSN: 1525-2027

Ensemble inversion of time-dependent core flow models

N. Gillet
LGIT, University Joseph Fourier, CNRS, BP 53, F-38041 Grenoble CEDEX 9, France (nicolas.gillet@obs.ujf-grenoble.fr)

M. A. Pais
CFC, Department of Physics, University of Coimbra, 3004-516 Coimbra, Portugal (pais@teor.fis.uc.pt)

D. Jault
LGIT, University Joseph Fourier, CNRS, BP 53, F-38041 Grenoble CEDEX 9, France (dominique.jault@obs.ujf-grenoble.fr)

[1] Quasi-geostrophic core flow models are built from two secular variation models spanning the periods 1960–2002 and 1997–2008. We rely on an ensemble method to account for the contributions of the unresolved small-scale magnetic field interacting with core surface flows to the observed magnetic field changes. The different core flow members of the ensemble solution agree up to spherical harmonic degree $\ell \simeq 10$, and this resolved component varies only weakly with regularization. Taking into account the finite correlation time of the small-scale concealed magnetic field, we find that the time variations of the magnetic field occurring over short time scales, such as the geomagnetic jerks, can be accounted for by the resolved (large-scale) part of the flow to a large extent. Residuals from our flow models are 30% smaller for recent epochs, after 1995. This result is attributed to an improvement in the quality of geomagnetic data. The magnetic field models show little frozen flux violation for the most recent epochs, within our estimate of the apparent magnetic flux changes at the core-mantle boundary arising from spatial resolution errors. We associate the more important flux changes detected at earlier epochs with uncertainties in the field models at large harmonic degrees. Our core flow models show, at all epochs, an eccentric and planetary-scale anticyclonic gyre circling around the cylindrical surface tangent to the inner core, at approximately 30 and 60 latitude under the Indian and Pacific oceans, respectively. They account well for the changes in core angular momentum for the most recent epochs.

Components: 10,916 words, 14 figures, 2 tables.

Keywords: geomagnetic secular variation; core flows.

Index Terms: 1530 Geomagnetism and Paleomagnetism: Rapid time variations; 1213 Geodesy and Gravity: Earth's interior: dynamics (1507, 7207, 7208, 8115, 8120).

Received 20 October 2008; **Revised** 7 April 2009; **Accepted** 14 April 2009; **Published** 10 June 2009.

Gillet, N., M. A. Pais, and D. Jault (2009), Ensemble inversion of time-dependent core flow models, *Geochem. Geophys. Geosyst.*, *10*, Q06004, doi:10.1029/2008GC002290.

1. Introduction

[2] Large and medium scales of core surface flows have been captured as the result of the continuous observation of the large-scale (harmonic degree $\ell \leq 13$) Earth's magnetic field from low Earth orbiting satellites since 1999 [*Holme and Olsen*, 2006]. Unfortunately, from the Earth surface upward, the small-scale magnetic field $\tilde{\mathbf{B}}$ ($\ell > 13$) originating from the core is difficult to isolate: its intensity at higher degrees becomes weaker than that of the lithospheric field. The small-scale core field is much stronger at the core surface, where it interacts significantly with the medium scales of the flow and contributes to the large-scale secular variation (SV) [*Hulot et al.*, 1992]. This SV signal corresponds to spatial resolution errors, sometimes called errors of representativeness in the data assimilation community [*Kalnay*, 2003]. Both *Eymin and Hulot* [2005] and *Pais and Jault* [2008] relied on a stochastic approach to quantify it at discrete times. They found that the spatial resolution errors dominate the error budget for the large length-scale secular variation.

[3] Ensemble methods are routinely used in atmospheric forecasting to produce estimates for the complete probability density of the state variable [*Wunsch*, 2000]. Ensemble forecasting helps improve the forecast by ensemble averaging, and provides an indication of the reliability of the forecast [*Kalnay*, 2003, p. 236]. We remark that ensemble methods are suitable to quantify the contribution of the concealed $\tilde{\mathbf{B}}$ interacting with the surface core flow to the observed large-scale SV. Using an ensemble method makes it straightforward to account for the time variability of $\tilde{\mathbf{B}}(t)$. We anticipate that improving our knowledge of the time properties of the secular variation signal that results from the advection of $\tilde{\mathbf{B}}$ may help alleviate its impact on the calculation of the large-scale core surface flow. Typical time scales for the magnetic field structures have been derived from the ratio of the SV and main field spectra [*Hulot and Le Mouël*, 1994]. Extrapolating those spectra, as obtained from time-dependent field models, one finds that $\tilde{\mathbf{B}}$ typically has correlation times of the order of 20 years and below for harmonic degrees above 13. It is thus reasonable to suppose that its advection entails spatial resolution errors that are correlated in time. We test this idea and generate an ensemble of core flow solutions from an ensemble of small-scale magnetic fields $\tilde{\mathbf{B}}$ correlated in time.

[4] All discussions on core dynamics relying on observations of magnetic field time changes are potentially affected by the spatial resolution errors that we seek to quantify. As an example, the observed temporal variations of the unsigned magnetic flux are often interpreted as evidence for magnetic diffusion [*Gubbins and Bloxham*, 1985]. It is not easy, however, to disentangle the respective contributions of magnetic diffusion, and that of induction involving the unresolved magnetic field, to the changes in magnetic flux at the core surface. Another example is the suggestion [*Bloxham et al.*, 2002] that geomagnetic jerks may result from the interaction between torsional Alfvén waves and the radial magnetic field at the core mantle boundary (CMB). According to *Bloxham et al.* [2002], differences in the geometry of the radial magnetic field from one place to the other explain the observation that geomagnetic jerks are seen in some components at some observatories but not detected in others. We shall investigate first which component of the large-scale core flow accounts for the rapid changes of the magnetic field, once time correlation of spatial resolution errors is taken into account, and secondly whether spatial resolution errors have more impact on magnetic series in some observatories than in others.

[5] The setup of our core flow inverse problem is detailed in section 2. We calculate quasi-geostrophic time-dependent core flows from two SV models covering annual to decadal time scales: the comprehensive model CM4 [*Sabaka et al.*, 2004], which covers 1960–2002, and the model xCHAOS [*Olsen and Mandea*, 2008], derived from satellite data and annual differences of monthly means over the period 1997–2008. The amplitude of the spatial resolution errors, their time correlation and SV predictions from our different flow models at location of magnetic observatories are discussed in section 3. Estimates of the changes in the magnetic flux through the main reverse flux patch (beneath South Atlantic) associated with the spatial resolution errors are then carried out in section 4. The computed core flows are described in section 5, where a comparison with independent length of day data is also carried out. Finally, in section 6 we discuss the perspectives for the core flow inverse problem.

2. Methodology

2.1. Formalism and Notations

[6] Vectors $\mathbf{m}$, $\mathbf{y}$ and $\mathbf{x}$ store the spherical harmonic coefficients for the main magnetic field, secular

variation, poloidal and toroidal scalars of the core surface flow model, respectively. The "data" $\mathbf{y}$ (and their associated errors $\mathbf{e}$) are linked to the core flow model $\mathbf{x}$, at every epoch t, via the forward problem

$$\mathbf{y}(t) = \mathsf{A}[\mathbf{m}(t)]\,\mathbf{x}(t) + \mathbf{e}, \tag{1}$$

corresponding to the frozen flux radial induction equation at the CMB [e.g., *Holme*, 2007]

$$\frac{\partial B_r}{\partial t} = -\nabla_h \cdot (\mathbf{u} B_r). \tag{2}$$

[7] We choose to truncate the secular variation data set at harmonic degree $\ell_\mathsf{y} = 13$. The main field $\mathbf{m} = [\overline{\mathbf{m}}, \tilde{\mathbf{m}}]$ is composed of a large-scale part $\overline{\mathbf{m}}$ obtained from published geomagnetic field models (up to degree $\overline{\ell}_\mathsf{m} = 13$), and a small-scale part $\tilde{\mathbf{m}}$ (degrees $\overline{\ell}_\mathsf{m} < \ell \leq \ell_\mathsf{m}$) estimated with a stochastic approach (section 2.3). We truncate the core flow model at $\ell_\mathsf{x} = 26$ [*Pais and Jault*, 2008], a degree high enough to include interactions between $\overline{\mathbf{m}}$ and $\mathbf{x}$ possibly generating secular variation at $\ell \leq \ell_\mathsf{y}$. The truncation level for $\tilde{\mathbf{m}}$ is chosen as $\ell_\mathsf{m} = 40$, a degree high enough to include interactions between $\tilde{\mathbf{m}}$ and $\mathbf{x}$ possibly generating secular variation at $\ell \leq \ell_\mathsf{y}$. The vectors sizes of $\mathbf{m}$, $\mathbf{y}$ and $\mathbf{x}$ at a single epoch are then $N_\mathsf{m} = \ell_\mathsf{m}(\ell_\mathsf{m} + 2)$, $N_\mathsf{y} = \ell_\mathsf{y}(\ell_\mathsf{y} + 2)$ and $N_\mathsf{x} = 2\ell_\mathsf{x}(\ell_\mathsf{x} + 2)$, respectively.

[8] The null space of the forward problem (1) being very large, some extra constraint is needed [*Backus*, 1968]. For short time scale dynamics, the ratio between Lorentz and Coriolis forces is also the ratio between the frequencies of Alfvén and inertial waves, and can be estimated by the *Lehnert* [1954] number $\lambda = B/\Omega c\sqrt{\rho\mu_0}$ [*Jault*, 2008], where c is the outer core radius, ρ the core density, μ_0 the permeability of free space, Ω the rotation rate, and B is an estimate of the magnetic field strength. B is typically of a few mT inside the core, on the basis of a long time scale force balance [*Starchenko and Jones*, 2002], which gives $\lambda \sim 10^{-4} \ll 1$. This motivates the use of the quasi-geostrophic (QG) hypothesis, a constraint which allows a flow invariant parallel to the rotation axis $\mathbf{z}$ to be described everywhere in the outer core. It implies the tangential geostrophy (TG) constraint $\nabla_h \cdot (\mathbf{u}\cos\theta) = 0$ at the CMB [*Hills*, 1979; *Le Mouël*, 1984], plus nonpenetration at the tangent cylinder (the cylinder tangent to the inner core and aligned with the rotation axis) and equatorial symmetry outside the tangent cylinder [*Pais and Jault*, 2008]. We decompose the core flow as $\mathbf{u} = \mathbf{u}_e + u_z\hat{\mathbf{z}}$. The z-invariant equatorial component $\mathbf{u}_e$ of the flow can be defined with a stream function $\psi(s, \phi, t)$ as

$$\mathbf{u}_e(s, \phi, t) = \nabla \times (\mathbf{z}\psi). \tag{3}$$

The description of the flow is completed by the expression of its axial component

$$u_z(s, \phi, z, t) = \frac{-sz}{H(s)^2} u_s(s, \phi, t), \tag{4}$$

which ensures the nonpenetration condition at the CMB, with (s, ϕ, z) the cylindrical coordinates and $H(s) = \sqrt{c^2 - s^2}$ the half-height of a fluid column.

[9] There exists a basis of flow vectors that automatically satisfy the TG constraint [*Le Mouël et al.*, 1985; *Backus and Le Mouël*, 1986]. The flow coefficients $\mathbf{w}$ in that basis are related to the coefficients $\mathbf{x}$ in the toroidal/poloidal expansion through the orthogonal matrix G:

$$\mathbf{x}(t) = \mathsf{G}\,\mathbf{w}(t). \tag{5}$$

The number of unknowns for a single epoch is then reduced to $N_\mathsf{w} = \ell_\mathsf{x}{}^2$ the size of the vector $\mathbf{w}$ [*Jackson*, 1997]. We denote $\mathsf{H}(t) = \mathsf{A}(t)\,\mathsf{G}$ the matrix relating the flow coefficients $\mathbf{w}$ to the SV coefficients $\mathbf{y}$.

[10] We follow *Jackson* [1997] for the implementation of the time-dependent problem [see also *Bloxham and Jackson*, 1992]. The core flow coefficients are expanded in terms of a basis of cubic B splines functions $F_p(t)$ [*Lancaster and Salkauskas*, 1986] uniformly spanning the time interval $[t_s, t_e]$ with knot-spacing Δt:

$$\mathbf{w}(t) = \sum_{p=1}^{P} F_p(t)\,\mathbf{w}^p. \tag{6}$$

We denote $\mathbf{W}$ the vector $[\mathbf{w}^1 \ldots \mathbf{w}^P]$ and $\mathbf{X}$ the vector $[\mathbf{x}^1 \ldots \mathbf{x}^P]$, with $\mathbf{x}^p = \mathsf{G}\mathbf{w}^p$. We sample the time span $[t_s, t_e]$ with steps δt. At every epoch t_j we estimate the main field coefficients $\mathbf{m}(t_j) = \overline{\mathbf{m}}(t_j) + \tilde{\mathbf{m}}(t_j)$ needed to build the interaction matrices $\mathsf{A}(t_j)$ (see section 2.3), and the data coefficients $\mathbf{y}(t_j) = \frac{\partial \overline{\mathbf{m}}}{\partial t}(t_j)$. From the latter we generate a data vector $\mathbf{Y} = [\mathbf{y}(t_s) \ldots \mathbf{y}(t_e)]$, a combined set of SV Gauss coefficients calculated at each time step, associated with the error vector $\mathbf{E} = [\mathbf{e}(t_s) \ldots \mathbf{e}(t_e)]$. The forward problem is now written $\mathbf{Y} = \mathcal{H}\mathbf{W} + \mathbf{E}$, where $\mathcal{H}$ is a banded matrix with bandwidth $4N_\mathsf{w}$, calculated from the interaction matrices $\mathsf{H}(t_j) = \mathsf{A}(t_j)\,\mathsf{G}$ and the value $F_p(t_j)$ taken by each B spline F_p at epoch t_j.

[11] The solution of our problem is found by minimizing the objective function

$$J(\mathbf{W}) = \| \mathbf{Y} - \mathcal{H}\mathbf{W} \|^2_{\mathsf{C_y}} + \xi \| \mathbf{W} \|^2_{\mathsf{Q_w}} + \mu \| \mathbf{W} \|^2_{\mathsf{P_w}}, \quad (7)$$

with the generic notation $\| \mathbf{V} \|^2_{\mathsf{M}} = \mathbf{V}^T \mathsf{M}^{-1} \mathbf{V}$. The first term is $\chi^2 = \| \mathbf{Y} - \mathcal{H}\mathbf{W} \|^2_{\mathsf{Cy}}$, a measure of the misfit to the SV data, with the data covariance matrix $\mathsf{C_y}$ as detailed in section 2.2. The second term is a spatial regularization of the flow model, with ξ a damping parameter tuned to adjust the compromise between a reasonable model complexity and a good fit to the data. The third term corresponds to the equatorial symmetry and nonpenetration constraints at the tangent cylinder, imposed using a weak form with μ a parameter big enough so that these constraints are practically satisfied. The damping matrix $\mathsf{Q_w}$, together with the constraint matrices $\mathsf{P_w}$, are defined in section 2.2. Minimizing the cost function J, as defined in equation (7), is a linear optimization problem. Its solution is

$$\mathbf{W} = \left[\mathcal{H}^T \mathsf{C_y}^{-1} \mathcal{H} + \xi \mathsf{Q_w}^{-1} + \mu \mathsf{P_w}^{-1} \right]^{-1} \mathcal{H}^T \mathsf{C_y}^{-1} \mathbf{Y}. \quad (8)$$

In practice, δt = 1 year and P = 24, which corresponds to a knot spacing Δt = 2 years, are used to invert the CM4 SV coefficients spanning $[t_s, t_e]$ = [1960, 2002]. Convergence of the solution with δt has been checked for. Similarly, δt = 0.5 year and P = 25 are used to invert the xCHAOS SV coefficients over the time span $[t_s, t_e]$ = [1997, 2008] (i.e., a knot spacing Δt = 0.5 year). Finally, we derive $\mathbf{x}(t)$ from $\mathbf{W}$ using equations (5) and (6).

2.2. Regularization, Constraints, and Error Model

[12] The norm used throughout our study to regularize the problem is

$$\mathcal{Q}_3(\mathbf{u})^2 = \left\langle \int_{\mathsf{CMB}} (\mathcal{D}^2 + \mathcal{V}^2) \mathbf{ds} \right\rangle = (t_e - t_s)^{-1} \| \mathbf{W} \|^2_{\mathsf{Q_w}} = (t_e - t_s)^{-1} \| \mathbf{X} \|^2_{\mathsf{Q_x}}, \quad (9)$$

with the horizontal divergence $\mathcal{D} = \nabla_h \cdot \mathbf{u}$ and the radial vorticity $\mathcal{V} = \hat{\mathbf{r}} \cdot \nabla \times \mathbf{u}$. The angular brackets denote the time-averaging operator:

$$\langle \rangle = \frac{1}{t_e - t_s} \int_{t_s}^{t_e} dt. \quad (10)$$

The matrix $\mathsf{Q_x}^{-1}$ is bloc-diagonal, with elements varying with harmonic degree ℓ as $[\ell(\ell+1)]^2/(2\ell+1) \propto \ell^3$, and $\mathsf{Q_w}^{-1} = \mathsf{G}^T \mathsf{Q_x}^{-1} \mathsf{G}$. The extra linear constraints in (7), namely, the equatorial symmetry and nonpenetration at the tangent cylinder, are calculated as in the work by *Pais and Jault* [2008]. They can be written in the form $\mathsf{L}\,\mathbf{x} = \mathsf{L}\,\mathsf{G}\,\mathbf{w} = 0$, which yields $\mathsf{P_w}^{-1} = \mathsf{G}^T \mathsf{L}^T \mathsf{L} \mathsf{G}$. In practice the parameter μ is large enough so that increasing it does not affect the solution.

[13] Other quadratic norms could have been used, such as the minimum energy norm [*Madden and Le Mouël*, 1982; *Pais et al.*, 2004]

$$\mathcal{Q}_1(\mathbf{u})^2 = \left\langle \int_{\mathsf{CMB}} \| \mathbf{u} \|^2 \ \mathbf{ds} \right\rangle \propto \frac{\ell(\ell+1)}{2\ell+1} \sim \ell^1, \quad (11)$$

which gives the RMS velocity $\mathcal{Q}_1$ and corresponds to a relatively weaker damping of the high harmonic degrees, or the more severe and widely used "strong norm" [*Bloxham*, 1988; *Jackson et al.*, 1993; *Jackson*, 1997]

$$\mathcal{Q}_5(\mathbf{u})^2 = \left\langle \int_{\mathsf{CMB}} \left(\| \nabla_h \mathcal{D} \|^2 + \| \nabla_h \mathcal{V} \|^2 \right) \mathbf{ds} \right\rangle \propto \frac{[\ell(\ell+1)]^3}{2\ell+1} \sim \ell^5. \quad (12)$$

Our norm $\mathcal{Q}_3(\mathbf{u})^2$ scales as ℓ^3, as does the strongest component of the norm used by *Pais and Jault* [2008] (symmetric part of the Reynolds tensor).

[14] We assume that the errors are stationary and that the data covariance matrix is diagonal. We denote $\sigma^{\mathsf{d}^2}(\ell) = E[\mathsf{e}^{\mathsf{d}^2}_{\ell m}]$ the data covariances, which are independent of the spherical harmonic order m (isotropic errors). Supposing that the energy of the data error spreads uniformly over all harmonic degree (i.e., flat Lowes spectrum), one obtains a bloc-diagonal covariance matrix $\mathsf{C_y}$ of which elements are the variances $\sigma^{\mathsf{d}^2}(\ell) = \eta/(\ell+1)(2\ell+1)$. The *a priori* noise level is set at η = 0.4 (nT/a)^2 for both the CM4 and xCHAOS models. This choice is somewhat arbitrary, and a better description of both the spatial and temporal statistical behavior of data errors could be useful in future work. First, there are some hints that the coefficients of the data covariance matrix should depend on $\ell - m$ to account for a poor knowledge of the magnetic field in auroral regions [*Olsen and Mandea*, 2007]. Secondly the use of a temporal regularization to generate time-dependent field models reduces the time variability of the SV coefficients at high degrees, penalizing the

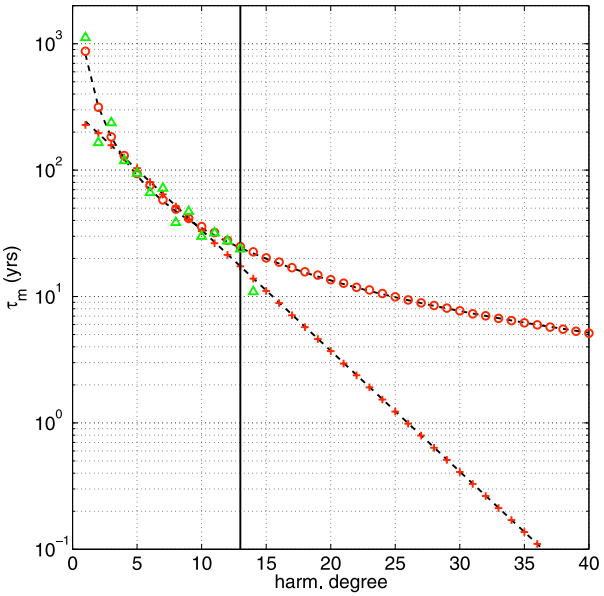

Figure 1. The main field correlation time τ_m as a function of harmonic degree ℓ, estimated from the ratio $R(\ell)$ for the GRIMM model at epoch 2003.5 (green triangles), its exponential and power law fits (dotted black), and calculated from the synthetic time series (red circles, power law fit; red crosses, exponential fit). Only harmonic degrees above $\ell = 13$ (to the right of the vertical line) are used in the ensemble inversion.

instantaneous secular acceleration $\frac{\partial^2 B_r}{\partial t^2}$ at small scales. There is indeed a trade-off between the spatial complexity and the temporal variability of a magnetic field model. *Olsen and Mandea* [2008] gave precedence to the former over the latter, as noted by *Lesur et al.* [2008] who also remarked that the secular acceleration predicted by xCHAOS is fully controlled by the regularization process above degree 11. Introducing time correlation in the data errors (nondiagonal covariance matrix, i.e., $E[\mathsf{e}^{\mathsf{d}}_{\ell m}(t)\mathsf{e}^{\mathsf{d}}_{\ell m}(t \pm \tau)] \neq 0$) or a time-correlated noise at small scales (e.g., with an ensemble approach for the data errors) might be a way to address this issue.

2.3. Small-Scale Magnetic Field With Zero Mean and Gaussian Time Correlation Function

[15] An ensemble of K matrices A^k is calculated from an ensemble of K small-scale magnetic fields $\tilde{\mathbf{m}}^k$. We consider the small-scale field as a random noise with a Gaussian centered time correlation. A set of K random small-scale main field models $\tilde{\mathbf{m}}^k(t)$ is generated, satisfying: $\forall k \in [1, K]$, $\forall \ell \in [\bar{\ell}_m, \ell_m]$, $\forall m \leq \ell$, $\forall (t, t') \in [t_s, t_e]^2$,

$$E\left[\tilde{\mathbf{m}}^k_{\ell m}(t), \tilde{\mathbf{m}}^k_{\ell m}(t')\right] = \sigma^2_{\mathsf{m}}(\ell) \exp\left[-\frac{1}{2}\left(\frac{t-t'}{\tau_{\mathsf{m}}(\ell)}\right)^2\right], \quad (13)$$

where $\tilde{\mathbf{m}}^k_{\ell m}(t)$ denotes a coefficient of degree ℓ and order m of the spherical harmonic expansion of the magnetic field at epoch t. $E[\ldots]$ represents the mathematical expectation, $\tau_{\mathsf{m}}(\ell)$ is the typical correlation time for the main field coefficients of degree ℓ and $\sigma^2_{\mathsf{m}}(\ell)$ their variance. The choice of a stationary Gaussian correlated stochastic process is justified by the work of *Hulot and Le Mouël* [1994]. It reflects the statistical behavior of both the observed historical and archeomagnetic fields [*Hongre et al.*, 1998].

[16] In order to estimate the variances $\sigma^2_{\mathsf{m}}(\ell) = E[\tilde{\mathbf{m}}_{\ell m}(t)^2]$, we fit an exponential curve to the Lowes spectrum of the main field model GRIMM [*Lesur et al.*, 2008] for degrees $\ell \in [2, 13]$, epoch 2003.5, and extrapolate it for degrees $\ell > 13$. It gives $\sigma^2_{\mathsf{m}}(\ell) = 1.09 \times 10^9 e^{-1.26\ell}/(\ell + 1)(2\ell + 1)$. For each degree ℓ, typical correlation times $\tau_{\mathsf{m}}(\ell)$ for the main field are estimated from SV and main field spectra [*Hulot and Le Mouël*, 1994],

$$R(\ell) = \tau_{\mathsf{m}}(\ell)^{-2} = \left[\sum_{m \leq \ell}\left(g^2_{\ell m} + h^2_{\ell m}\right)\right]^{-1} \sum_{m \leq \ell}\left(\dot{g}^2_{\ell m} + \dot{h}^2_{\ell m}\right), \quad (14)$$

where the upper "dot" denotes the time derivative. A power law fit for harmonic degrees $\ell \leq 11$ of GRIMM at 2003.5 gives $R(\ell) \simeq 1.47 \times 10^{-6}\ell^{2.75}$ a^{-2}. Its extrapolation gives estimates from 22 to 5 years for harmonic degrees 14 to 40 of $\tilde{\mathbf{B}}$. As mentioned in section 2.2, the SV coefficients are likely to be too much correlated at high degrees, because of temporal regularization of time-dependent field models. Thus the choice of a power law fit to $R(\ell)$ is questionable [see, e.g., *Holme and Olsen*, 2006], and we also tried the case of an exponential fit to $R(\ell)$ for $\ell \in [2, 11]$. We obtain $R(\ell) \simeq 1.1 \times 10^{-5} e^{0.44\ell}$, that is τ_{m} from 14 to 0.05 years for harmonic degrees 14 to 40 of $\tilde{\mathbf{B}}$. In this latter case the small scales are much less correlated in time, as illustrated in Figure 1. Figure 1 also shows that our synthetic coefficient time series, computed by low-pass filtering a random noise, have correlation times very close to what is requested. These time series are normalized in order to have the required variance $\sigma^2_{\mathsf{m}}(\ell)$, and sampled every δt to produce the coefficients $\tilde{\mathbf{m}}_{\ell m}(t_j)$.

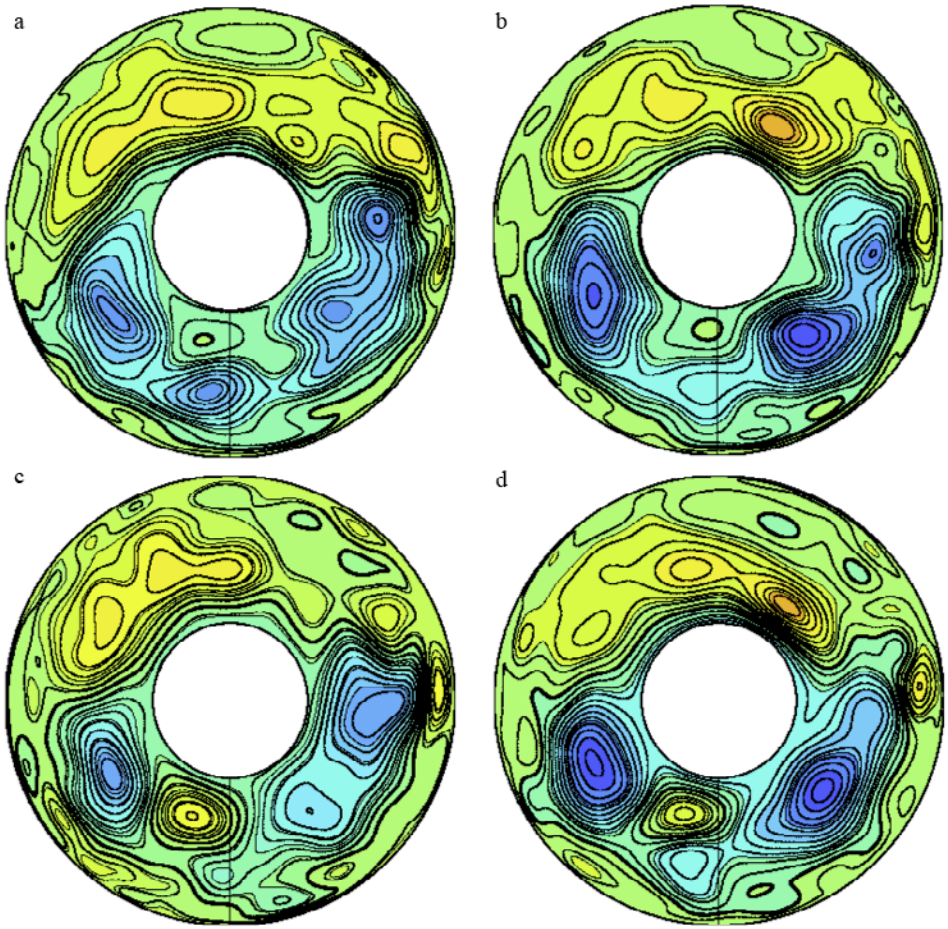

Figure 2. Snapshots of the stream function ψ in the equatorial plane outside the tangent cylinder, viewed from the North Pole, for several models $\mathbf{x}^k$ of the ensemble solution, from CM4 at epoch 1980, for $\xi = 10^{-3}$ and $\tau_{\mathsf{m}}(\ell)$ estimated with an exponential fit to $R(\ell)$. The color scale ranges between ±8 (dimensionless units), with contours every 0.4 and the zero contour in bold. The blue (yellow) areas correspond to anticyclonic (cyclonic) circulations. The thin black radial line corresponds to the projection of the Greenwich meridian on the equatorial plane.

[17] We concatenate the large-scale main field coefficients with the small-scale random ones into an ensemble of K models $\mathbf{m}^k(t) = [\overline{\mathbf{m}}(t), \tilde{\mathbf{m}}^k(t)]$. From these, we generate K matrices

$$\mathsf{A}^k(t) = \mathsf{A}[\mathbf{m}^k(t)] = \overline{\mathsf{A}}(t) + \tilde{\mathsf{A}}^k(t), \tag{15}$$

where we can separate the mean interaction matrix $\overline{\mathsf{A}}(t) = \mathsf{A}[\overline{\mathbf{m}}(t)]$ and $\tilde{\mathsf{A}}^k(t) = \mathsf{A}[\tilde{\mathbf{m}}^k(t)]$ since the operator A is linear. Matrices A^k are used to invert for K flow models $\mathbf{x}^k$, as detailed in section 2.1. The choice of the damping parameter ξ is such that the normalized misfit to the data $\mathcal{M} = \sqrt{\frac{\chi^2}{PN_{\mathbf{y}}}}$, the first term in the cost function J defined in equation (7), is of order unity for each of the individual models $\mathbf{x}^k$.

3. Accounting for Rapid Changes in the Secular Variation

3.1. Ensemble of Flow Solutions

[18] Figure 2 illustrates several core flow solutions from the ensemble of models $\mathbf{x}^k$ at the epoch 1980 (from CM4). Local features of the flows vary widely from one model to the other: see for instance the cyclonic (yellow) patch to the west of the Greenwich meridian, the location of the maximal cyclonic vorticity in the Pacific hemisphere, or the variability in the intensity of the anticyclonic (blue) vortices in the Atlantic hemisphere. It illustrates how the ignorance of the small-scale magnetic field $\tilde{\mathbf{B}}$ bears upon the solution of the core flow inverse problem. This

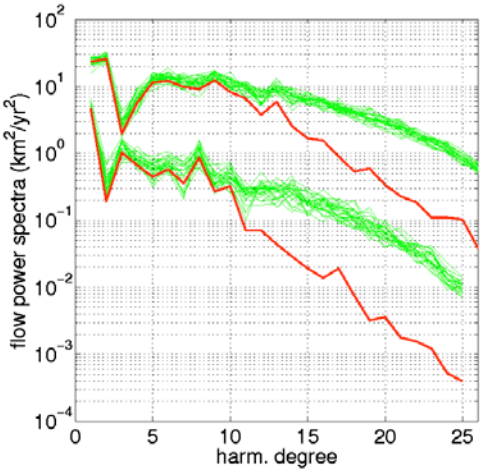

Figure 3. Time averaged toroidal $\mathcal{E}_t$ (top set of curves) and poloidal $\mathcal{E}_s$ (bottom set of curves) CMB flow power spectra for the ensemble of models $\mathbf{x}^k$ (green) and the average $\hat{\mathbf{x}}$ (red), from CM4, for $\xi = 10^{-3}$ and $\tau_{\mathsf{m}}(\ell)$ estimated with an exponential fit to $R(\ell)$.

dispersion means that most of the small length-scale vortices are not resolved.

[19] In Figure 3, the CMB flow spectra for models $\mathbf{x}^k$ are compared to the spectrum for the mean model

$$\hat{\mathbf{x}}(t) = \frac{1}{K}\sum_{k=1}^{K}\mathbf{x}^k(t), \tag{16}$$

Averaged solutions are calculated using $K = 25$ realizations of $\tilde{\mathbf{B}}$, which, as we checked, is enough to obtain a converged average model $\hat{\mathbf{x}}$. The time averaged kinetic energy spectra $\mathcal{E}_s$ ($\mathcal{E}_t$) for the poloidal (toroidal) components of the flow are defined as

$$\{\mathcal{E}_s(\ell),\mathcal{E}_t(\ell)\} = \left\langle \frac{\ell(\ell+1)}{2\ell+1}\sum_{m\le\ell}\left\{ s^s_{\ell m}(t)^2 + s^c_{\ell m}(t)^2, t^s_{\ell m}(t)^2 + t^c_{\ell m}(t)^2 \right\}\right\rangle,$$

where the $\{s^{s,c}_{\ell m}, t^{s,c}_{\ell m}\}$ are the poloidal and toroidal spherical harmonic flow coefficients [e.g., *Holme*, 2007], with the notation $\langle\ldots\rangle$ defined in equation (10). Above harmonic degree 10 or so, the mean flow becomes less and less energetic compared to any of the individual realizations: small-scale flow structures cancel out from one inversion to the other. The agreement between the different individual solutions below degree 10 means that the (large-scale) average over the ensemble of flow solutions can be considered as a resolved component of the core flow. In Figure 2, it essentially corresponds to an eccentric planetary-scale anticyclonic gyre that shows a dichotomy between the Atlantic and Pacific hemispheres, with a few large- to medium-scale vortices superimposed on it (see section 5).

[20] Figure 4 illustrates that the average solution $\hat{\mathbf{x}}$ (still for CM4) depends only weakly on the choice of the damping parameter ξ. This result contrasts with the stronger dependence on ξ of the snapshot flow solutions previously calculated [e.g., *Pais and Hulot*, 2000; *Eymin and Hulot*, 2005]. *Jackson* [1997] found that the RMS velocity of his time-dependent flow solution increases by a factor of 30% as the damping parameter ξ is divided by 10. In our study, the RMS flow velocity (the norm $\mathcal{Q}_1$, see Table 1) for the average solution $\hat{\mathbf{x}}$ calculated from CM4 changes only by 3% as ξ is divided by 10, whereas individual solutions $\mathbf{x}^k$ change by about 20%. The dependence on ξ of the norm $\mathcal{Q}_3$ used to penalize the high degrees is larger, with 23% and 50% evolutions for $\hat{\mathbf{x}}$ and the $\mathbf{x}^k$, respectively. The conventional solution, chosen according to some criterion about the misfit on a trade-off curve, depends strongly on the *a priori* choice of an error model which is poorly documented. Our new approach to calculate resolved core flows can also be compared to the

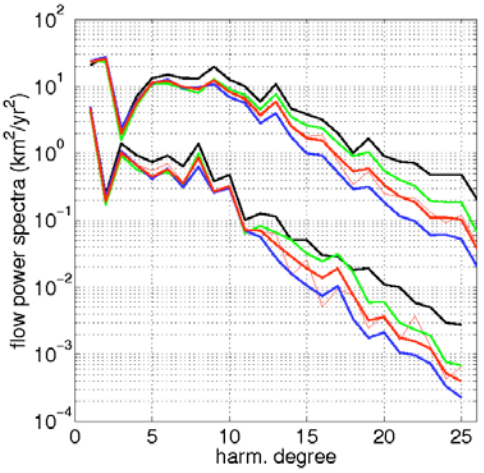

Figure 4. Time averaged toroidal $\mathcal{E}_t$ (top set of curves) and poloidal $\mathcal{E}_s$ (bottom set of curves) CMB flow power spectra for the average models $\hat{\mathbf{x}}$ inverted from CM4, for several models of $\tilde{\mathbf{B}}$ and different damping parameters ξ. Time correlated $\tilde{\mathbf{B}}$ with $\tau_{\mathsf{m}}(\ell)$ estimated with an exponential fit to $R(\ell)$ and three different values of $\xi = 3\times10^{-4}$ (bold green), 10^{-3} (bold red), and 3×10^{-3} (bold blue). Time correlated $\tilde{\mathbf{B}}$ with $\tau_{\mathsf{m}}(\ell)$ estimated with a power law fit to $R(\ell)$ and $\xi = 10^{-3}$ (thin red). Bold black indicates uncorrelated $\tilde{\mathbf{B}}$ and $\xi = 3\times10^{-4}$.

Table 1. Comparison of Different Flow Inversions Considered in This Study[a]

SV Model	Time Correlation	ξ	$\hat{\mathcal{M}}$	$\mathcal{M}(\hat{\mathbf{x}})$	$\hat{\mathcal{Q}}_3$	$\mathcal{Q}_3(\hat{\mathbf{x}})$	$\hat{\mathcal{Q}}_1$	$\mathcal{Q}_1(\hat{\mathbf{x}})$
CM4	white	$3\ 10^{-4}$	1.54	5.35	17.96	10.39	18.01	14.30
CM4	Gaussian (pow)	$1\ 10^{-3}$	1.52	6.40	12.34	7.73	14.68	12.41
CM4	Gaussian (exp)	$3\ 10^{-4}$	1.02	6.56	15.16	8.57	16.13	12.57
CM4	Gaussian (exp)	$1\ 10^{-3}$	1.57	6.33	12.41	7.81	14.76	12.45
CM4	Gaussian (exp)	$3\ 10^{-3}$	2.35	6.31	10.09	6.98	13.59	12.18
xCHAOS	Gaussian (exp)	$3\ 10^{-4}$	0.48	5.36	14.93	8.29	16.54	13.49
xCHAOS	Gaussian (exp)	$1\ 10^{-3}$	0.73	5.09	12.31	7.60	15.57	13.55
xCHAOS	Gaussian (exp)	$3\ 10^{-3}$	1.06	4.88	10.38	7.04	14.86	13.52
xCHAOS	Gaussian (exp)	$1\ 10^{-2}$	1.59	4.82	8.66	6.45	14.16	13.34
xCHAOS	Gaussian (exp)	$3\ 10^{-2}$	2.37	5.06	7.28	5.85	13.47	12.99

[a] $\hat{\mathcal{M}}$, $\hat{\mathcal{Q}}_3$, and $\hat{\mathcal{Q}}_1$ stand for the average over the K realizations of the misfit and the norms, respectively. The RMS velocity $\mathcal{Q}_1$ is given in km a^{-1}. The norm $\mathcal{Q}_3$ (homogeneous to the RMS radial vorticity) is given in 10^{-5} d^{-1}. The abbreviations "pow" and "exp" stand for "exponential" and "power law" fit to the ratio $R(\ell)$, respectively.

method recently put forward by two of us [*Pais and Jault*, 2008]. They developed an inversion scheme where the spatial resolution errors were estimated iteratively. Results were similar in that much the kinetic energy of the largest scales of the flow did not depend on the *a priori* error model. They differed to the extent that the harmonic degree above which regularization strongly reduced the flow amplitude varied with the error model (compare, e.g., *Pais and Jault*'s [2008] Figure 7 (left) and Figure 7 (right)). Our results give credit to the ensemble approach, where the calculated solutions are much less sensitive to the initial error model and to the choice of the free parameter ξ, as shown in Table 1.

[21] In the same Figure 4, we also compare spectra of average flow solutions $\hat{\mathbf{x}}$ calculated from several models of $\tilde{\mathbf{B}}$, either presenting no time correlation (bold black), or with time correlation $\tau_{\mathsf{m}}(\ell)$ estimated from an exponential (bold red) or a power law (thin red) fit to $R(\ell)$ (see section 2.3). For an ensemble of flow solutions presenting a similar misfit $\mathcal{M}^k$ to the data in all cases, using a small-scale magnetic field model $\tilde{\mathbf{B}}$ independent from one epoch to the other increases the energy and the complexity of the solution $\hat{\mathbf{x}}$. This means that the advection of an uncorrelated $\tilde{\mathbf{B}}$ is less able to account for the observed smooth variation of the field. Hence, we have a first indication that time correlation of $\tilde{\mathbf{B}}$ matters. However, one can notice that the *a priori* choice of scaling for $\tau_{\mathsf{m}}(\ell)$ does not strongly affect the average flow solution $\hat{\mathbf{x}}$.

[22] We have also tested the effect of weaker and stronger norms, imposing damping matrices with diagonal elements proportional to ℓ^1 and ℓ^5, respectively (see section 2.2). Using a stronger (weaker) norm brings more energy into larger (smaller) scales for the mean solution $\hat{\mathbf{x}}$ (for the ensemble of models $\mathbf{x}^k$ each presenting a misfit $\mathcal{M}^k \simeq 1$ in all cases). We observe that the unresolved flow at high degrees (the part which varies from one realization to the other) is relatively less important for a strong norm than for a weak norm: the dispersion of the ensemble of flow solutions is smaller with a strong norm. As we require in both cases the ensemble of individual flow models to fit the data well, using a strong norm generates an average solution which can account for a larger part of the signal than using a weak norm does. The robust character of our flow solutions, which depends only weakly on the value of the damping parameter ξ, is nevertheless conditional on the definition of the norm $\| \ldots \|_{\mathsf{Q_w}}$. However, the main conclusions derived in the next sections about the statistical properties of the spatial resolution errors, the fit to geophysical data, the planetary-scale anticyclonic gyre, and the magnetic diffusion are not qualitatively affected by this *a priori* choice.

3.2. Statistical Properties of the Spatial Resolution Errors

[23] Because of underparameterization of the forward problem, most previous studies try to explain all the observed SV as an effect of a large-scale field $\overline{\mathbf{B}}$ being advected by a large-scale flow. As a result, some aliasing occurs over the large-scale flow coefficients [*Celaya and Wahr*, 1996]. Here we try to circumvent this difficulty using a stochastic model for $\tilde{\mathbf{B}}$ and allowing the individual flows that fit the SV data to have smaller scales.

[24] We define the spatial resolution errors $\mathbf{e}^{\mathbf{r}}$ as the difference between (1) the predictions resulting

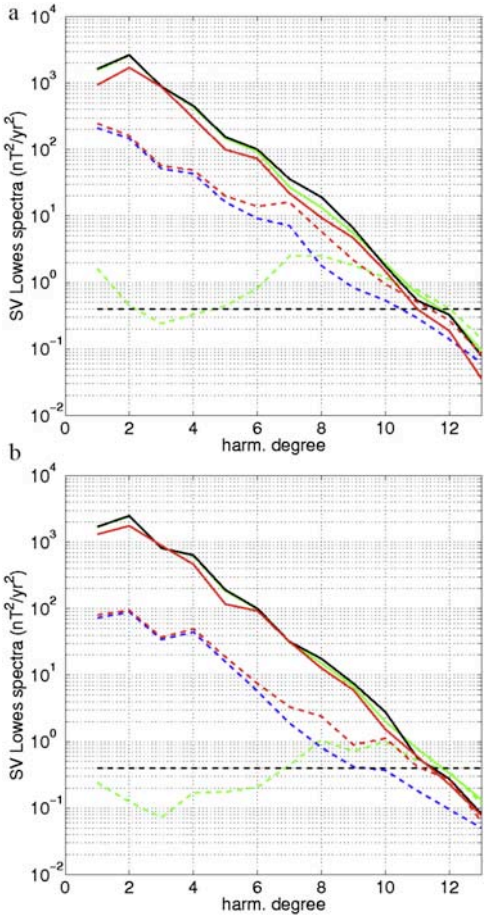

Figure 5. Time averaged SV Lowes spectra at the Earth surface, from (top) CM4 ($\xi = 10^{-3}$) and (bottom) xCHAOS ($\xi = 3 \times 10^{-3}$): data (black) and noise level (dotted black), average predictions (green), average prediction errors (dotted green), and average spatial resolution errors (dotted blue) over the ensemble of models $\mathbf{x}^k$, predictions (red) and prediction errors (dotted red) for $\hat{\mathbf{x}}$. The correlation times $\tau_{\mathsf{m}}(\ell)$ of $\tilde{\mathbf{B}}$ are calculated with an exponential fit to $R(\ell)$.

from the average and resolved flow model $\hat{\mathbf{x}}$ interacting with the "known" large-scale main field $\overline{\mathbf{m}}$ and (2) the predictions from each $\mathbf{x}^k$ interacting with its associated $\mathbf{m}^k = \overline{\mathbf{m}} + \tilde{\mathbf{m}}^k$:

$$\mathbf{e}^{\mathbf{r}k} = \overline{\mathsf{A}}\,\hat{\mathbf{x}} - \mathsf{A}^k\,\mathbf{x}^k, \tag{18}$$

with the matrices $\overline{\mathsf{A}}$ and A^k as defined in section 2.3.

[25] Our method for estimating the effect of the unresolved magnetic field differs from that of *Eymin and Hulot* [2005] and *Pais and Jault* [2008]. These two studies aimed at estimating the spatial resolution errors in order to recover the largest scales of the core flow in a consistent way. In the work by *Pais and Jault* [2008], the spatial resolution errors were added to the observation errors in the objective function (see its definition (7) in our case), so that they contribute to condition the computed flow. Instead, we estimate the spatial resolution errors ex post facto in order to quantify the predicting power of the average flow solution $\hat{\mathbf{x}}$ and to discuss their stationarity.

[26] We first discuss the spatial properties of the error budget, before its temporal characteristics are analyzed. Figure 5 shows the time averaged SV Lowes spectra at the Earth's surface (radius a = 6371.2 km) for the data, the model predictions and prediction errors, for an ensemble inversion using the CM4 (Figure 5, top) and xCHAOS (Figure 5, bottom) magnetic field models. As required by our choice of the damping parameter (see section 2.2 and below), any of the individual flow models $\mathbf{x}^k$ accounts well for the SV data: the energy of the prediction errors from the several $\mathbf{x}^k$ is much smaller than that of the SV signal for harmonic degrees $\ell < 11$ for CM4 and $\ell < 12$ for xCHAOS. The mean velocity model $\hat{\mathbf{x}}$ is less able to account for the observed SV as it includes much fewer small scales at harmonic degrees $\ell > 10$.

[27] In agreement with what *Pais and Jault* [2008] found for the snapshot core flow inverse problem, the spatial resolution errors $\mathbf{e}^{\mathbf{r}}$ strongly dominate the error budget at the low harmonic degrees, whereas the noise level η from the data errors $\mathbf{e}^{\mathbf{d}}$ becomes important at higher degrees. We estimate the time average variances of the spatial resolution errors per harmonic degree, averaged over the K realizations, as

$$\sigma^{\mathsf{r}}(\ell)^2 = \frac{1}{2\ell+1}\sum_{m\le\ell}\frac{1}{K}\sum_{k=1}^{K}\langle \mathbf{e}^{\mathbf{r}k}_{\ell m}(t)^2\rangle, \tag{19}$$

using the notation (10). They can be fitted as $\sigma^{\mathsf{r}2}(\ell) \simeq \sigma_0^{\mathsf{r}2}\exp(-\ell)$, with $\sigma_0^{\mathsf{r}2}$ = 53 $(\mathrm{nT/a})^2$ for CM4, and 29 $(\mathrm{nT/a})^2$ for xCHAOS; note that the Lowes spectra of the spatial resolution error in Figure 5 is given by $(\ell+1)(2\ell+1)\,\sigma^{\mathsf{r}}(\ell)^2$. We observe that the prediction errors spectrum dominates that of the spatial resolution errors for $\ell \ge 8$ for both CM4 and xCHAOS (see the green and blue dotted curves in Figure 5), a degree above which spatial resolution errors become relatively less important. Our estimate of σ_0^{r} for xCHAOS is in agreement with the findings of *Pais and Jault* [2008] from the closely related CHAOS model [*Olsen et al.*, 2006]. The larger time averaged

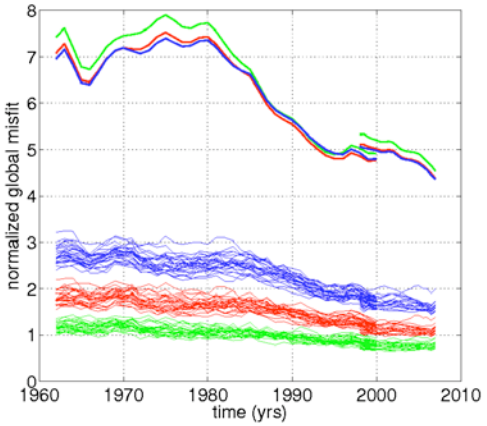

Figure 6. Normalized misfit to the data (CM4 continued by xCHAOS) $\mathcal{M}^k$ associated with the ensemble of flows $\mathbf{x}^k$ (thin curves) and $\mathcal{M}$ $(\hat{\mathbf{x}})$ associated with the average flow solution $\hat{\mathbf{x}}$ (bold curves), calculated for several damping parameters increasing from green to blue: ξ = (0.3, 1,3) $\times$ 10^{-3} (CM4) and ξ = (1, 3,10) $\times$ 10^{-3} (xCHAOS). The correlation times $\tau_{\mathsf{m}}(\ell)$ of $\tilde{\mathbf{B}}$ are calculated with an exponential fit to $R(\ell)$.

values of $\sigma^{\mathsf{r}}(\ell)^2$ found for CM4 than for xCHAOS illustrate that the average model $\hat{\mathbf{x}}$ is able to better account for the xCHAOS SV than for the CM4 SV, at least over the full time span $[t_s, t_e]$ of these models. That suggests that the time average accuracy of xCHAOS is better than that of CM4. We now concentrate on the time variation of the spatial resolution errors.

[28] Figure 6 shows that the normalized residuals $\mathcal{M}^k$ for the flow models $\mathbf{x}^k$ inverted from CM4 gradually decrease with time, by about 30% after say 1975 (thin curves). We attribute this result to a gradual improvement in data quality with time, with the Magsat satellite mission in 1980 and the increasing accuracy in the observatory measurements over the past 50 years (see section 6). The normalized prediction errors $\mathcal{M}$ $(\hat{\mathbf{x}})$ for the average model $\hat{\mathbf{x}}$ interacting with the large-scale magnetic field $\overline{\mathbf{m}}$ (which is a good approximation of the normalized spatial resolution errors at low degrees: see Figure 5, dotted red and blue curves) also shows a 30% drop between 1980 and 1995: our resolved large-scale flow better accounts for the observed secular variation after 1990 than before 1980. We suspect we may be underestimating the data errors in the first half of the time span (as we considered stationary data errors $\mathbf{e}^{\mathbf{d}}$ for simplicity), and thus map part of $\mathbf{e}^{\mathbf{d}}$ into the spatial resolution errors. Interestingly, the misfit for the average model $\mathcal{M}$ $(\hat{\mathbf{x}})$ found at the end of CM4 matches well that found for the starting epochs of xCHAOS (note that the *a priori* choice of noise level is similar for both models): it seems that the accuracy of both models is somewhat similar for the time interval during which they overlap. We can as well detect a significant decrease of the prediction errors for $\hat{\mathbf{x}}$ over the satellite era. We have no explanation for this result, except for the first 2 years of xCHAOS, which are not constrained by satellite data but by observatory monthly means only. Finally, note that the time evolution of the residuals for the average model $\hat{\mathbf{x}}$ is only slightly affected by our choice of damping parameter ξ, as can be seen in Figure 6.

[29] We calculate for each spherical harmonic coefficient the time correlation of the spatial resolution errors as an average over the K realizations:

$$\rho^{\mathsf{r}}_{\ell m}(\tau) = \frac{1}{K}\sum_{k=1}^{K} \frac{\int_{t_s}^{t_e-\tau} \left[\mathbf{e}^{\mathbf{r}k}_{\ell m}(t) - \langle \mathbf{e}^{\mathbf{r}k}_{\ell m}\rangle\right]\left[\mathbf{e}^{\mathbf{r}k}_{\ell m}(t+\tau) - \langle \mathbf{e}^{\mathbf{r}k}_{\ell m}\rangle\right] dt}{(t_e - t_s - \tau)\left\langle \left[\mathbf{e}^{\mathbf{r}k}_{\ell m}(t) - \langle \mathbf{e}^{\mathbf{r}k}_{\ell m}\rangle\right]^2 \right\rangle}, \tag{20}$$

with the notation $\langle \ldots \rangle$ of equation (10). For simplicity, the spatial resolution errors are assumed stationary (but see the discussion above). Figure 7 presents the calculated $\rho^{\mathsf{r}}_{\ell m}(\tau)$ for all harmonic coefficients. We find no obvious dependence of $\rho^{\mathsf{r}}_{\ell m}(\tau)$ on the degree ℓ, the order m or $(\ell - m)$. Some dispersion in both the correlation time (from 5 to 15 a) and the shape of the correlation function is observed for the SV coefficients for which the spatial resolution errors dominate the residuals of individual inversions ($\ell \leq 8$). The coefficients of higher degree are correlated as well, over similar time scales, with very little dispersion.

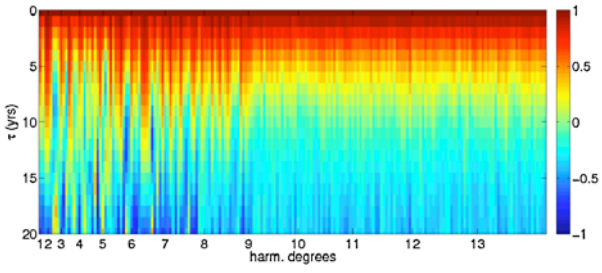

Figure 7. Correlation $\rho^{\mathsf{r}}_{\ell m}(\tau)$ for the spatial resolution errors as defined in equation (20), from CM4, with ξ = 10^{-3} and an exponential fit to $R(\ell)$ for the estimation of $\tau_{\mathsf{m}}(\ell)$. The harmonic degree value is indicated in the horizontal axis, and all coefficients within a certain ℓ are listed in the following order: $\dot{g}^0_1$, $\dot{g}^1_1$, $\dot{h}^1_1$, $\dot{g}^0_2$, $\dot{g}^1_2$, $\dot{h}^1_2$, $\dot{g}^2_2$, $\dot{h}^2_2$, $\dot{g}^0_3$ ... $\dot{g}^{13}_{13}$, $\dot{h}^{13}_{13}$.

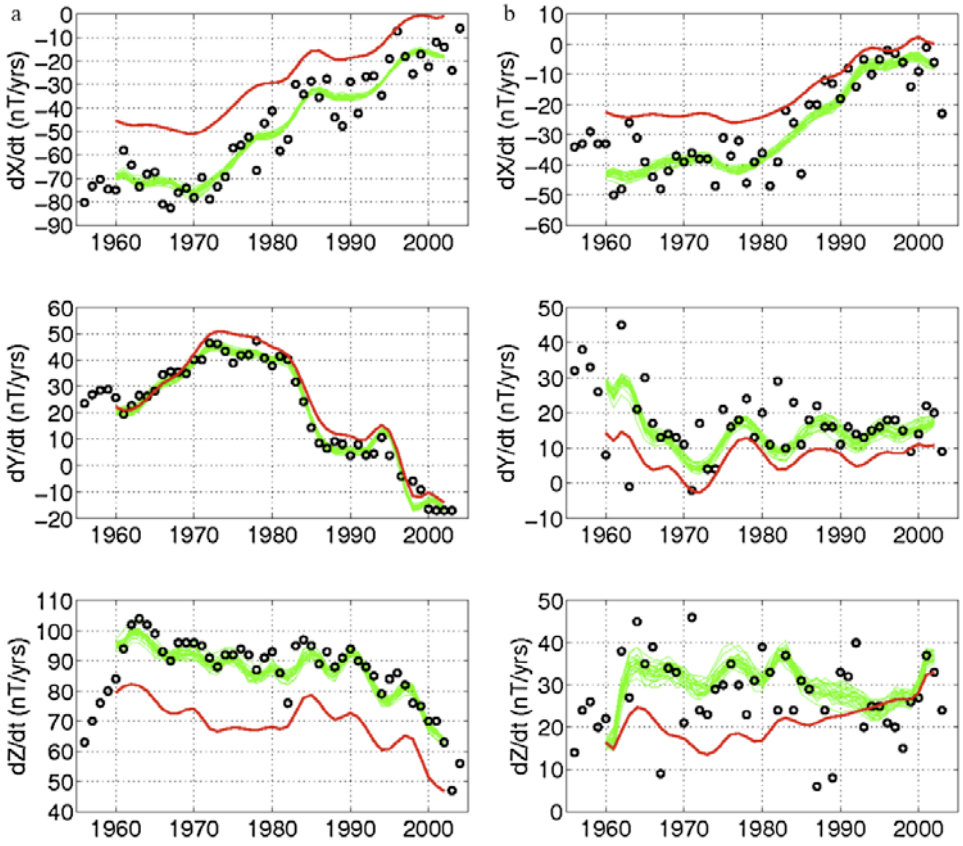

Figure 8. X, Y and Z components of the secular variation annual means (black circles) at (left) the Hermanus observatory (South Africa) and (right) the Macquarie Island observatory (Australia), superimposed on model predictions for the ensemble of models $\mathbf{x}^k$ (green) and the average model $\hat{\mathbf{x}}$ (red), from CM4, with $\xi = 10^{-3}$ and an exponential fit to $R(\ell)$ for the estimation of $\tau_{\mathrm{m}}(\ell)$.

[30] We have now a clear assessment of the statistical properties of spatial resolution errors. On the one hand, they have variances $\sigma^{\mathrm{r}}(\ell)^2$ large enough to yield a significant misfit between SV data and predictions from the resolved core flow interacting with the large-scale magnetic field. On the other hand, the finite correlation time, of the order of 10 years, of the spatial resolution errors implies that this misfit does not change abruptly, but slowly evolves over subdecade time scales. There is more information to be collected in the temporal changes of the SV data, which we can attribute to rapid changes of the flow, rather than in their absolute level, which has an important contribution from (time correlated) nonlinear interactions involving small length scales features. Specifically, rapid changes in the SV such as geomagnetic jerks should be well predicted by the resolved part of our core flow models.

3.3. SV at Observatory Location

[31] In Figures 8 and 9we compare our flow model predictions inferred from CM4 with the SV annual mean data at the observatories in Hermanus (South Africa), Macquarie Island (Australia), Kakioka (Japan) and Niemegk (Germany). All models $\mathbf{x}^k$ fit the data well (green curves). It means that it is possible to account for the observatory data with rather energetic QG flows presenting numerous small structures (see section 5). The less energetic average flow does not fit the data as well as the individual realizations $\mathbf{x}^k$ do (red curve). Note that the average of the predictions from the $\mathbf{x}^k$ is not the prediction of the mean flow $\hat{\mathbf{x}}$, because it is not a linear function of the small-scale field $\tilde{\mathbf{B}}$.

[32] Typically, the prediction of $\hat{\mathbf{x}}$ is less than the observed SV (at least for most cases where the amplitude of the SV signal is large). As a consequence, the residuals from the averaged model $\hat{\mathbf{x}}$, and thus the spatial resolution errors, tend to be correlated with the SV data. In other words, the average model $\hat{\mathbf{x}}$ fails to predict part of the highs

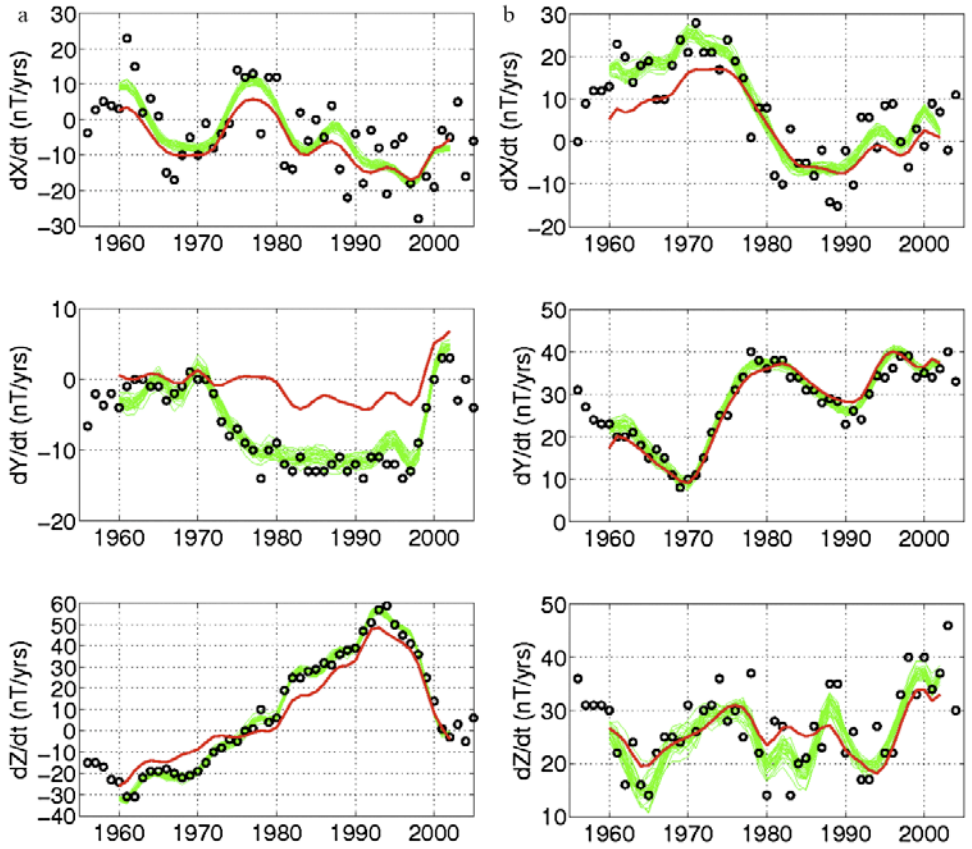

Figure 9. Same as Figure 8 at (left) the Kakioka observatory (Japan) and (right) the Niemegk observatory (Germany).

and lows on a map of the SV at the Earth's surface. Our estimates of $\hat{\mathbf{x}}$ act as a low-pass filter of the actual velocity at the core surface, keeping only the large length scales of the flow but with gain probably less than one.

[33] As we anticipated, the flow $\hat{\mathbf{x}}$ accounts much better for the temporal changes of the magnetic field SV recorded in the observatories than for its amplitude; see, e.g., the almost constant shift, on all three components, between the observations and the $\hat{\mathbf{x}}$ prediction at Hermanus, from both CM4 (Figure 8) and xCHAOS (Figure 10). The characteristic signature of geomagnetic jerks can be well reproduced from our robust QG flow model (all three components at Niemegk, Y component at Hermanus, Z component at Kakioka). In another instance, the rapid changes in the 1970s and around 2000 are missing (Y component in Kakioka, but see the weak amplitude of the signal at that epoch). Note that all three components at Niemegk, located in a region where there are many magnetic observatories, are well reproduced. Figure 10 shows flow model predictions inferred from xCHAOS with annual differences of both annual and monthly means at Niemegk and Hermanus observatories (the latter have been collated by *Chulliat and Telali* [2007]). They are shown in the geomagnetic dipole coordinate system (X_d, Y_d, Z_d), rather than in the geographic frame (X, Y, Z) = (North, East, Down), in order to reduce the scatter of the monthly means data due to external field sources, and thus facilitate the comparison. Our models can account rather well for the rapid changes reported by *Olsen and Mandea* [2007, 2008] on the Y_d component at Niemegk (around 2003 and 2005) and at Hermanus (in 2005), where the amplitude of the signal is much larger. The wiggle of similar amplitude, observed on the Z_d component at Hermanus around 2003, is not modeled by the xCHAOS magnetic model, and thus cannot be reproduced by our ensemble of flow model predictions.

4. On a Possible Misinterpretation of Apparent Frozen Flux Violation

[34] Magnetic diffusion, as a source of modeling errors in calculation of core surface flows, has been much studied [see *Holme and Olsen*, 2006, and

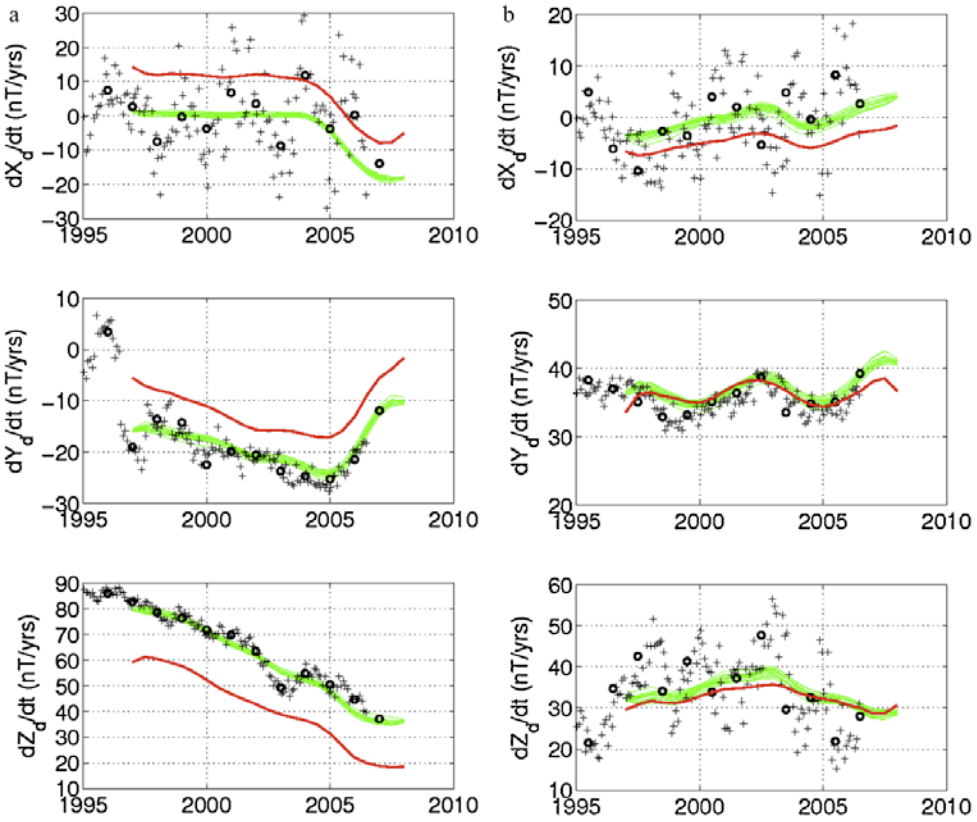

Figure 10. Annual differences of annual (black circles) and monthly (black crosses) means in geomagnetic dipole coordinate (X_d, Y_d, Z_d) at (left) the Hermanus observatory (South Africa) and (right) the Niemegk observatory (Germany), superimposed with model predictions for the ensemble of models $\mathbf{x}^k$ (green) and the average model $\hat{\mathbf{x}}$ (red), from xCHAOS, with $\xi = 3 \times 10^{-3}$ and an exponential fit to $R(\ell)$ for the estimation of $\tau_{\mathsf{m}}(\ell)$.

references therein]. Let us assume that the time correlation of the errors arising because of magnetic diffusion can be directly inferred from the time correlation τ_{m} of the observed magnetic field (see section 2.3). The latter time decreases, as a function of harmonic degree, from a few hundred years for $\ell = 2$ down to about 20 years for $\ell = 13$. According to this reasoning, magnetic diffusion cannot hinder the identification of the core flow features responsible for the rapid changes of the magnetic field.

[35] In this section, we aim to estimate how much of the apparent signature of diffusion observed in the main field models is associated with the SV induced by the spatial resolution errors. The frozen flux approximation leads to conservation laws [*Backus*, 1968] on the magnetic flux through surfaces $\mathcal{S}$ bounded by material curves $\mathcal{C}$ on which $B_r = 0$:

$$\frac{d}{dt}\int_{\mathcal{S}} B_r \, \mathbf{ds} = \frac{d}{dt}\int_{\mathsf{CMB}} |B_r| \mathbf{ds} = 0. \tag{21}$$

However, we do not have access to the actual null-flux curves $\mathcal{C}$, since they are influenced by the small-scale field $\tilde{B}_r$ and only the large-scale field $\overline{B}_r$ is known. The technique to detect magnetic diffusion at the CMB has then been to monitor the time evolution of the flux of magnetic field through patches $\overline{\mathcal{S}}$ bounded by the curves $\overline{\mathcal{C}}$ where $\overline{B}_r = 0$ [*Bloxham et al.*, 1989]. From the induction equation (2) projected onto the subspace of large-scale components ($\ell \leq 13$), and allowing for prediction errors from the inverted flows, one finds

$$\frac{\partial \overline{B}_r}{\partial t} = -\overline{\nabla_h \cdot \left(\mathbf{u}^k \left[\overline{B}_r + \tilde{B}_r^k\right]\right)} + \overline{\varepsilon^k}, \tag{22}$$

where $\overline{\varepsilon^k}$ represents the residual after the inversion for the individual flow $\mathbf{u}^k$ calculated from the realization $\tilde{B}_r^k$ of the small-scale magnetic field. The overbar denotes the projection on the spherical harmonic coefficients of degree $\ell \leq 13$. The frozen flux necessary condition through any patch $\overline{\mathcal{S}}$ is:

$$\int_{\overline{\mathcal{S}}} \left[\frac{\partial \overline{B}_r}{\partial t} + \overline{\nabla_h \cdot \left(\mathbf{u}^k \overline{B}_r\right)}\right] \mathbf{ds} = -\int_{\overline{\mathcal{S}}} \left[\overline{\nabla_h \cdot \left(\mathbf{u}^k \tilde{B}_r^k\right)} + \overline{\varepsilon^k}\right] \mathbf{ds}. \tag{23}$$

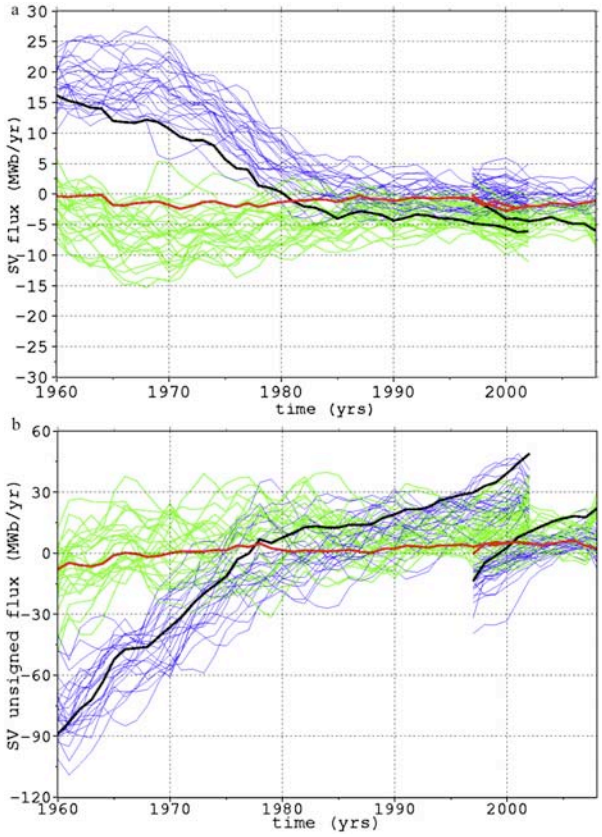

Figure 11. (top) Time variation of the SV flux through the Southern Hemisphere reverse flux patch (below South Atlantic and Indian Ocean). (bottom) Time variation of the total unsigned SV flux through the CMB. Black indicates flux calculated for the CM4 and xCHAOS models. Blue indicates flux associated with the residuals from the ensemble of flow models $\mathbf{x}^k$. Green indicates flux predicted from the flow models $\mathbf{x}^k$ advecting $\overline{\mathbf{m}} + \tilde{\mathbf{m}}^k$. Red indicates flux predicted from the average flow model $\hat{\mathbf{x}}$ advecting $\overline{\mathbf{m}}$. The correlation times $\tau_{\mathsf{m}}(\ell)$ of $\tilde{\mathbf{B}}$ are calculated with an exponential fit to $R(\ell)$. The damping parameters are $\xi = 10^{-3}$ (CM4) and $\xi = 3 \times 10^{-3}$ (xCHAOS).

[36] Neglecting the second term in the left-hand side and the right-hand side of equation (23) gives the condition which has been used as a test of frozen flux from magnetic field models [*Gubbins*, 1983]. We seek to quantify the importance of the extra terms in equation (23), in particular that involving the small-scale unresolved magnetic field $\tilde{B}_r$ and that related to the prediction errors $\overline{\varepsilon}$. We focus our study (Figure 11, top) on the reverse flux patch beneath South Atlantic and Indian oceans, which has given the main evidence for apparent frozen flux violation [*Bloxham et al.*, 1989; *Gubbins*, 2007]. In order to calculate flux integrals, we cover the region of interest with a triangulation on the unit sphere, and then use simple techniques to estimate integrals over each spherical triangle [*Renka*, 1997].

[37] On the left-hand side of equation (23), the surface integral of the divergence term involving the large-scale field $\overline{B}_r$ would be identically zero if all length scales of the divergence were allowed (because of the divergence theorem and using the fact that $\overline{B}_r = 0$ along each $\overline{\mathcal{S}}$ contour). We find (see the red curves of Figure 11) that it is effectively of much weaker amplitude than all other terms of equation (23). We find also (green curves in Figure 11, top) that the term involving the small-scale unresolved magnetic field in equation (23) is not the main contribution to the change of magnetic flux through the Southern Hemisphere reverse flux patch for the CM4 comprehensive model. It gives an error bar of the order of ±5 MWb/a on the flux integral variation resulting from the spatial resolution errors, for this specific reverse flux patch. Instead, residuals $\overline{\varepsilon^k}$ from our flow models (harmonic degrees $\ell = 10-13$) account for most of the observed violation of the frozen flux constraint (blue curves in Figure 11). Figure 5 indeed shows that the residuals from the flow models have the same energy as the CM4 SV model for these harmonic degrees. Figure 11 (top) also shows that the flux linked to this Southern Hemisphere patch changes much more slowly after 1980 than before. It is tempting to associate, once again, this observation with an improvement in the accuracy of magnetic field models for recent epochs: it may not be possible to resolve SV coefficients of degree $\ell = 10-13$ in the first half of the time interval covered by CM4. The variation in flux through the reverse flux patch for xCHAOS is weaker than that for CM4. It actually happens to be within the error bars estimated from the term involving the unresolved magnetic field, which means that we cannot derive yet a definitive conclusion about the actual presence of diffusion in the past decade.

[38] Studying the total unsigned flux, we reach the same conclusions. Dividing the CMB into I^+ patches $\overline{\mathcal{S}}_i^+$ where $\overline{B}_r > 0$, and I^- patches $\overline{\mathcal{S}}_i^-$ where $\overline{B}_r < 0$, we obtain from equation (23)

$$\int_{CMB} \left[\frac{\partial |\overline{B}_r|}{\partial t} + \overline{\nabla_h \cdot \left(\mathbf{u}^k |\overline{B}_r| \right)} \right] \mathbf{ds} = -\sum_{i=1}^{I^+} \int_{\overline{\mathcal{S}}_i^+} \left[\overline{\nabla_h \cdot \left(\mathbf{u}^k \tilde{B}_r^k \right)} \mathbf{ds} + \overline{\varepsilon^k} \right] \mathbf{ds} + \sum_{i=1}^{I^-} \int_{\overline{\mathcal{S}}_i^-} \left[\overline{\nabla_h \cdot \left(\mathbf{u}^k \tilde{B}_r^k \right)} + \overline{\varepsilon^k} \right] \mathbf{ds}. \quad (24)$$

It corresponds to the global unsigned flux conservation law. We computed the different contributing integrals in equation (24). The sign of the main field $\overline{B}_r$ at each point determines whether the cell corresponding to this point belongs to a flux patch $\overline{\mathcal{S}}_i^+$ or $\overline{\mathcal{S}}_i^-$. Figure 11 (bottom) shows that the residuals ε^k from the ensemble of flow models $\mathbf{x}^k$, rather than the induction term involving $\tilde{\mathbf{B}}^k$, account for the observed variation of the total unsigned flux for CM4. The latter only gives a lower bound for detectable decadal fluctuations of the global unsigned flux, of the order of ±20 MWb/a. The variations in the unsigned flux, as reconstructed from CM4, are much weaker after 1980. One cannot rule out the possibility of geomagnetic inverse problem side effects to explain this behavior: models such as CM4 or xCHAOS result from minimizing the time integral of both a misfit to the geomagnetic data and some norm of B_r at the CMB. Because the quantity and quality of the data vary in time, some artificial variation in the model complexity is generated, which implies artificial unsigned flux variations. These are particularly severe close to the endpoints, and the spatial norm of the model (hence the unsigned flux) typically reaches a minimum somewhere in the middle of the time interval. As a consequence, the SV unsigned flux evolves in time from negative to positive values, a characteristics which is observed for both the CM4 and xCHAOS models (see Figure 11, bottom).

[39] For CM4, the main source of flux variation detected in this study arises from residuals at high degrees, and not from the "subgrid-scale processes" modeled through the spatial resolution error. Our results then support the approach which consists in imposing constraints on the magnetic flux [*Constable et al.*, 1993; *O'Brien et al.*, 1998; *Jackson et al.*, 2007]. This was already a conclusion of *Bloxham et al.* [1989]. For field models built from spatially dense satellite data, such as xCHAOS, the reconstructed flux variation is within our estimate of the error bars because of the unresolved magnetic field.

5. Planetary-Scale Anticyclonic Gyre and Length of Day Variation

[40] Our averaged flow models $\hat{\mathbf{x}}$ show large- to medium-scale vortices superimposed on an eccentric and planetary-scale anticyclonic gyre (see the maps of the stream function in Figure 12). The vortices present for the satellite era were already found in the snapshot study by *Pais and Jault* [2008], with similar sign and location. However, it is worth noticing that their results show more small-scale features than ours. Two explanations can be offered. First of all, we remark above (Figure 4 and section 3.1) that taking into account the time correlation of $\tilde{\mathbf{B}}$ decreases the spatial complexity of the average flow. Inverting the flow at a single epoch, as *Pais and Jault* [2008] did, corresponds to neglecting the time correlation of $\tilde{\mathbf{B}}$. Secondly, these authors used a more complicated damping function: an extra soft constraint on u_s was imposed in order to represent the β effect characteristic of the quasi-geostrophic physics. Here we decided to use only one regularization (to avoid the use of two adjustable parameters). Eventually, a data assimilation framework may prove more appropriate to introduce dynamical constraints and to ponder the significance of small-scale vortices (see section 6).

[41] The planetary-scale anticyclonic gyre is almost tangent to the inner cylinder below the Pacific ocean, and flows at larger cylindrical radii below Asia (see Figure 12). This westward current, already described by *Pais and Jault* [2008], is particularly noticeable for the most recent epochs, for which it is modeled from the xCHAOS "data." There is a nice agreement between the flow models obtained from xCHAOS and that found at the end of the CM4 era around 2000. The variations in the core angular momentum, responsible for the observed length of day variation (LOD) [*Jault et al.*, 1988; *Jackson et al.*, 1993], are carried by small perturbations around this gyre.

[42] Flow model predictions of the LOD variation constitute an independent test involving the time changes of the toroidal coefficients t_1^0 and t_3^0 (but not their mean amplitude). As illustrated in Figure 13, we can see that the LOD variations for the most recent epochs (xCHAOS era) are well accounted for by our flow models. Moreover, the predictions are almost continuous around 2000 between the two models derived from CM4 and xCHAOS (the same shift, equivalent to a 9.5 ms potential LOD change, has been applied to all predictions from both magnetic models). However, the development of the gyre in the decade 1985–1995 corresponds to a large increase of the westward core angular momentum that is not matched by an increase of the eastward mantle angular momentum and consequent decrease of length of day, as inferred from the LOD data. The discrepancy is as large as 3 to 4 ms over almost 10 years. A similar difficulty has been reported by *Wardinski* [2004]. The use of

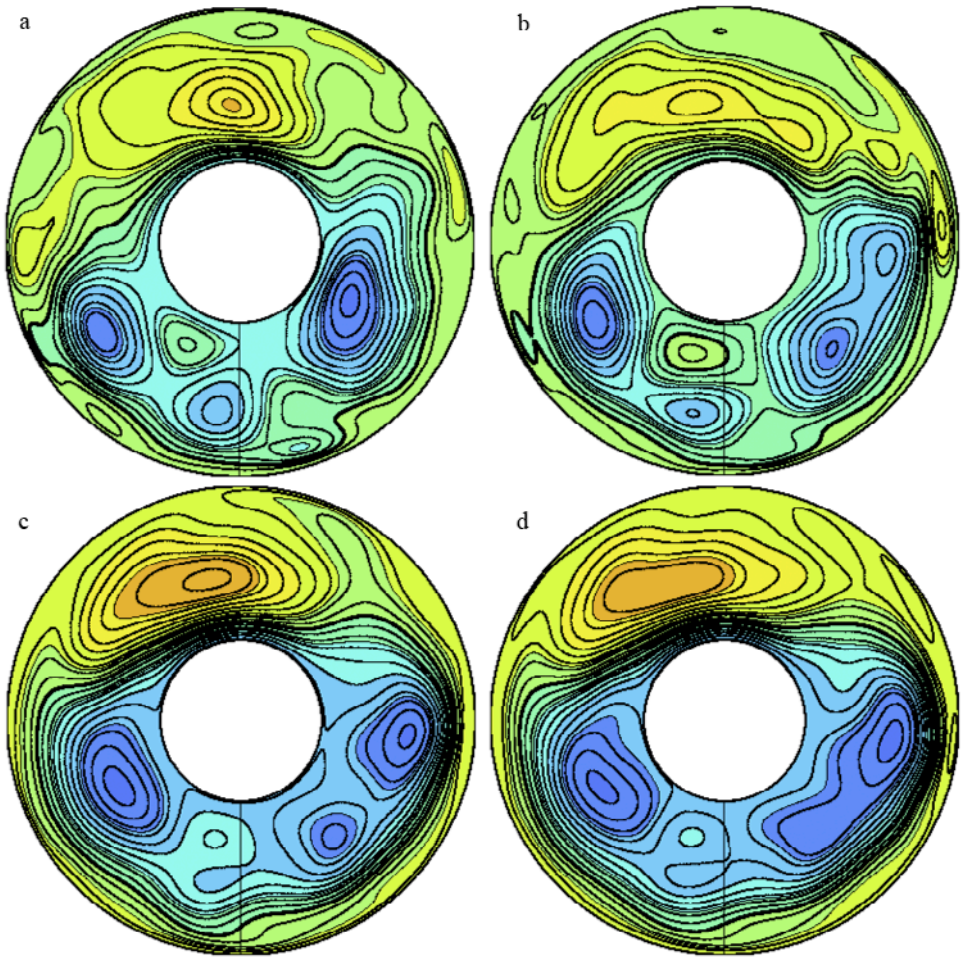

Figure 12. Snapshots of the stream function ψ in the equatorial plane outside the tangent cylinder, viewed from the North Pole, for the average model $\hat{\mathbf{x}}$ at several epochs. The color scale ranges between = ±8 (dimensionless units), with contours every 0.4 and the zero contour in bold. The blue (yellow) areas correspond to anticyclonic (cyclonic) circulations. The thin black radial line corresponds to the projection of the Greenwich meridian on the equatorial plane. The correlation times $\tau_{\mathrm{m}}(\ell)$ of $\tilde{\mathbf{B}}$ are calculated with an exponential fit to $R(\ell)$. The damping parameters are $\xi = 10^{-3}$ (CM4) and $\xi = 3 \times 10^{-3}$ (xCHAOS).

another model (C3FM [*Wardinski and Holme*, 2006]) and of a weaker constraint (TG only) only slightly help to reduce this mismatch. Figure 13 also illustrates the dispersion in the LOD model predictions over the ensemble of flow models $\mathbf{x}^k$. The predictions from almost all models are at odds with the LOD changes observed in the decade centered in 1990.

[43] The RMS flow velocities collected in Table 2 illustrate that our average flow models $\hat{\mathbf{x}}$ are dominated by their stationary component $\langle\hat{\mathbf{x}}\rangle$, amongst which the eccentric gyre. This stationary flow is composed of a nonnegligible zonal component $\langle\hat{\mathbf{x}}\rangle_0$, of which the RMS velocity is typically half that of the total flow. On the contrary, the time-variable flow $\hat{\mathbf{x}}' = \hat{\mathbf{x}} - \langle\hat{\mathbf{x}}\rangle$ is mainly composed of nonzonal velocity structures. For the calculations performed using xCHAOS over the period 1997–2008, which show a good fit to the LOD data, the RMS velocity of the time-variable axisymmetric flow $\hat{\mathbf{x}}'_0$ (responsible for the LOD variations) is only 28% that of $\hat{\mathbf{x}}'$. Our findings contrast with the scenario proposed by *Bloxham et al.* [2002], in which LOD variations and jerks detected at observatory locations are attributed to torsional oscillations superimposed on a stationary flow.

[44] We find a larger interannual variability for the flow models calculated from CM4 than from xCHAOS. The correlation between two stream function maps $\psi(s, \phi, t)$ obtained from xCHAOS at two different epochs (from 1998 to 2008) always exceeds 0.985. This value can be compared to 0.95, the correlation between the two stream function maps calculated from CM4 for the epochs

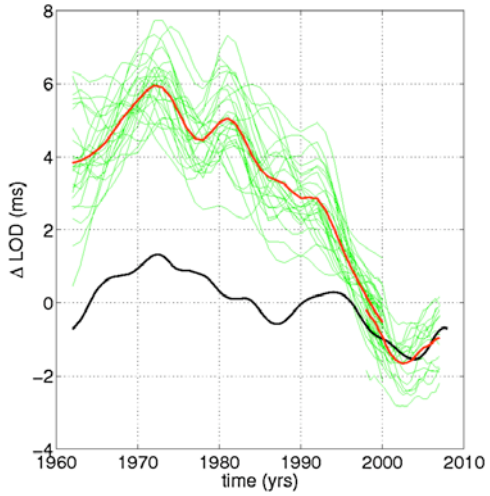

Figure 13. Length of day variations: data (black) and predictions from the ensemble of flow models $\mathbf{x}^k$ (green) and from the average model $\hat{\mathbf{x}}$ (red), from CM4 ($\xi = 10^{-3}$) and xCHAOS ($\xi = 3 \times 10^{-3}$), with $\tau_m(\ell)$ calculated with an exponential fit to $R(\ell)$. The same shift has been applied to all predictions from both magnetic models. The data are computed from the excess LOD (as provided by the Earth Orientation Center at the Paris Observatory, see http://hpiers.obspm.fr/eop-pc/) corrected from the atmospheric angular momentum (NCEP/NCAR reanalysis to obtain the effective angular momentum functions, see http://ftp.aer.com/pub/anon_collaborations/sba/). After a singular spectrum analysis decomposition, LOD variations are finally reconstructed from the first three empirical orthogonal functions using the SSA-MTM toolkit [*Ghil et al.*, 2002].

1990 and 2000. The lowest correlation between any two epochs of CM4, 0.82, corresponds to maps calculated for 1972 and 2002. We wonder whether some of the variability of the CM4 magnetic field model is spurious, as CM4 incorporates different types of data during its time span. It is possible also that xCHAOS shows too few fluctuations (because of a too heavily penalized secular acceleration, see section 2.2). Finally, there could be as well some real time variations in the amplitude of the nonstationary flow over the past 50 years.

[45] The eccentric gyre contains two regions of strong azimuthal flows respectively at radii $s \simeq 0.4$ (close to the tangent cylinder) and $s \simeq 0.85$ (near 30° latitude), a point which was already noted by *Pais and Jault* [2008] in their study of successive snapshots in 2001, 2002.5 and 2004. These two regions are connected by an ageostrophic flow (see the cylindrical radial flow below southeast Asia in Figure 12). The existence of such an ageostrophic flow over decadal time scales requires the magnetic field inside the outer core to be strong enough. Let us infer typical values for the internal magnetic field from a balance between Lorentz and Coriolis forces in the equation for the vertical vorticity, neglecting inertia:

$$\frac{2\rho\Omega s}{H(s)^2} u_s \sim \frac{1}{2\mu_0 H(s)} \int_{-H}^{+H} \mathbf{z} \cdot \nabla \times [(\nabla \times \mathbf{B}) \times \mathbf{B}]\, dz, \quad (25)$$

We further assume that **B** is essentially parallel to the gyre, i.e., frozen where the flow is the most rapid, in order to minimize induction. We note ($B_\perp$, $\delta_\perp$) and ($B_\parallel$, $\delta_\parallel$) the magnetic field components and their associated length scales, normal and tangent to the flow, respectively. Our local frozen flux hypothesis means that $B_\perp \ll B_\parallel$. Furthermore the solenoidal condition, for negligible gradients of B_z along the rotation axis, gives $\delta_\perp \sim \frac{B_\perp}{B_\parallel}\delta_\parallel \ll \delta_\parallel$, so that one can estimate the electrical currents as $\frac{B_\parallel}{\delta_\perp}$, and the Lorentz force in equation (25) as $\frac{B_\parallel B_\perp}{\delta_\perp^2}$. Such a balance gives the scaling law

$$B_\perp B_\parallel \sim 2\rho\mu_0\Omega \frac{s\delta_\perp^2 u_s^*}{H(s)^2}, \quad (26)$$

with $u^*_s \simeq$ 15 km/a the peak radial velocity along the gyre, and $\delta_\perp \simeq$ 250 km the half-width of the gyre estimated at this location. It gives a typical value of order 3 mT for the magnetic field $\sqrt{B_\perp B_\parallel}$ inside the core, an estimate ten times larger than the RMS value of B_r obtained at the CMB from geomagnetic models such as xCHAOS or CM4. Such an estimate compares well with that obtained with scaling laws derived from geodynamo models

Table 2. Time Averages of the RMS Flow Velocities $\mathcal{Q}_1$ for Average Flow Models $\hat{\mathbf{x}}$, Their Stationary Component $\langle\hat{\mathbf{x}}\rangle$, and Their Time-Dependent Component $\hat{\mathbf{x}}'$[a]

SV Model	Time Correlation	ξ	$\mathcal{Q}_1(\hat{\mathbf{x}})$	$\mathcal{Q}_1(\hat{\mathbf{x}}_0)$	$\mathcal{Q}_1(\langle\hat{\mathbf{x}}\rangle)$	$\mathcal{Q}_1(\langle\hat{\mathbf{x}}\rangle_0)$	$\mathcal{Q}_1(\hat{\mathbf{x}}')$	$\mathcal{Q}_1(\hat{\mathbf{x}}'_0)$
CM4	Gaussian (exp)	$1\ 10^{-3}$	12.45	5.78	10.99	5.24	6.06	2.45
xCHAOS	Gaussian (exp)	$3\ 10^{-3}$	13.52	7.66	13.40	7.62	2.32	0.65

[a] Flow velocities are in km a^{-1}. For each component, the values of the RMS axisymmetric flow (coefficients of order $m = 0$) is indicated with the subscript 0. For both the CM4 and xCHAOS SV "data," a representative flow model calculated with an intermediate damping parameter ξ (see Table 1) is illustrated, in the case of an exponential fit to the ratio $R(\ell)$.

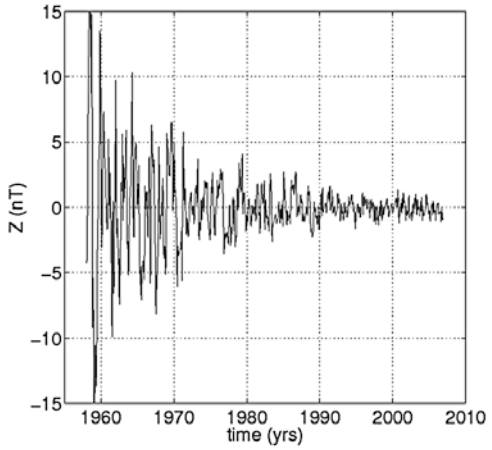

Figure 14. Difference between the Z components of the observatory monthly means as measured at Chambon-la-Forêt (CLF, France) and Dourbes (DOU, Belgium). The first two principal components have been removed to correct approximately for the magnetic field of internal origin. Taking the difference between two close-by observatories eliminates most of the large-scale external field, coherent over the few hundred km separating DOU and CLF. Noncoherent sources (e.g., induced fields in the lithosphere, small-scale ionospheric effects, etc.) as well as the noise of instrumental origin may still remain. It illustrates the improvement in the magnetic signal acquisition over the past 50 years. Data are from *Chulliat and Telali* [2007].

for two different force balances [*Starchenko and Jones*, 2002; *Christensen and Aubert*, 2006]. As a consequence it gives an estimate for the Alfvén waves period much shorter than that provided by *Zatman and Bloxham* [1997] from a torsional waves scenario (down to a few years instead of decades).

6. Conclusion

[46] The spatial resolution errors that we have investigated have correlation times of the order of 10 years. Thus, they do not hinder the identification of the flow structures that are at the origin of sudden changes in the SV, such as the geomagnetic jerks. We have found that the residuals from both the ensemble of our flow solutions and the averaged flow model decrease by about 30% during the 1980s. We think that this decrease originates from the gradual improvement of magnetic field models [*Hulot et al.*, 2007], which reflects the increased density and accuracy of magnetic observations. Declination/Inclination magnetometers (DI flux) became widely used in the observatories by the 1970s [*Turner et al.*, 2007]. The Magsat mission provided an accurate picture of the magnetic field for the year 1980. Together with the Oersted and CHAMP missions, it gave a good description of the average SV for the time interval 1980–1999. That motivated the development of a magnetic field model for the period 1980–2000: C3FM [*Wardinski and Holme*, 2006]. Finally, the Intermagnet network of digital observatories sharing modern measurement practices developed after 1990. Computing differences of magnetic field components recorded in two nearby observatories (CLF, France and DOU, Belgium) and removing decadal and interannual variations, the improvement is indeed manifest over the past 50 years, as illustrated in Figure 14. That operation eliminates the external signal coherent over the few hundred km separating the two observatories. The only possible explanation for the decrease of the variance of the series that we have constructed is a noise reduction with time (given that the noncoherent external and induced signals present smaller or stationary variances). We find it very encouraging that this improvement in data quality is reflected in an enhanced ability of our flow models to account for the observed SV.

[47] We have investigated whether apparent violations of the frozen flux constraints can be assigned to induction involving unresolved scales of the radial magnetic field at the CMB. We have found that these apparent violations were more likely caused by inaccuracies of high degree coefficients of the SV model CM4. Indeed, they are vanishing as SV models improve. Thus, our results give support to previous attempts at incorporating frozen flux constraints in geomagnetic field models [*Constable et al.*, 1993; *Jackson et al.*, 2007], at least before high-quality data have been recorded over a long time span. We stress, however, that quantifying apparent violations of the frozen flux constraints may eventually yield valuable upper bounds on subgrid-scale induction effects as data quality further improves.

[48] Introducing an ensemble approach and taking into account the time correlation of the concealed magnetic field, we have given a new twist to the kinematic approach, where SV models and core flows are calculated sequentially, making the core flow inverse problem linear. There have been earlier attempts to retrieve simultaneously a magnetic field and a flow model from observatory records [*Waddington et al.*, 1995]. Our observations concerning the fall of the misfit and of the apparent unsigned flux variation during the 1980s

and beyond, call for the introduction of data assimilation in magnetic field modeling. This technique, derived first for oceanography and meteorology [*Talagrand and Courtier*, 1987; *Talagrand*, 1997; *Ghil*, 1997] is able not only to retropropagate information toward epochs with poorer data coverage and/or accuracy, but also to satisfy constraints such as the frozen flux by using a dynamical model inside the penalty function. Using a simplified model and synthetic data, *Fournier et al.* [2007] have shown how dense and accurate measurements at the end of the time span of the model improves the model initial state after the assimilation process is completed. The apparent rapid changes of core angular momentum retrieved between 1985 and 1995 have no counterpart in LOD data. They are almost certainly spurious. This suggests that information constraining the evolution of the velocity field from the earlier epochs to the most recent ones, where our flow models account better for the observed magnetic field changes, is needed. Hopefully, our study will help to account better for the spatial resolution errors that will plague also the assimilation of magnetic field data obtained at the Earth's surface and above, in dynamical models of the Earth's core.

Acknowledgments

[49] We are indebted to Nils Olsen who provided us the magnetic field model xCHAOS. We are grateful to Andy Jackson for useful discussions and for providing the original B spline code for core flow inversions. We thank Henri-Claude Nataf and Thierry Alboussière for useful comments on the manuscript and Vincent Lesur, Gauthier Hulot, and an anonymous referee for reviews that helped improve the quality of the present work. The integrals of a scalar function over the sphere used John Burkardt's STRI-QUAD FORTRAN90 library (https://people.scs.fsu.edu/~burkardt). N.G. has been funded by a grant from the French Agence Nationale de la Recherche, Research program VS-QG (grant BLAN06-2.155316). This work has also been supported by the Cooperation Program PESSOA, between the Portuguese and French scientific agencies GRICES/EGIDE.

References

Backus, G. E. (1968), Kinematics of geomagnetic secular variation in a perfectly conducting core, *Philos. Trans. R. Soc. London, Ser. A*, *263*, 239–266.

Backus, G. E., and J.-L. Le Mouël (1986), The region on the core-mantle boundary where a geostrophic velocity field can be determined from frozen-flux magnetic data, *Geophys. J. R. Astron. Soc.*, *85*, 617–628.

Bloxham, J. (1988), The dynamical regime of fluid flow at the core-mantle boundary, *Geophys. Res. Lett.*, *15*, 585–588.

Bloxham, J., and A. Jackson (1992), Time-dependent mapping of the magnetic field at the core-mantle boundary, *J. Geophys. Res.*, *97*, 19,537–19,563.

Bloxham, J., D. Gubbins, and A. Jackson (1989), Geomagnetic secular variation, *Philos. Trans. R. Soc. London, Ser. A*, *329*, 415–502.

Bloxham, J., S. Zatman, and M. Dumberry (2002), The origin of geomagnetic jerks, *Nature*, *420*, 65–68.

Celaya, M., and J. Wahr (1996), Aliasing and noise in core-surface flow inversions, *Geophys. J. Int.*, *126*, 447–469.

Christensen, U. R., and J. Aubert (2006), Scaling properties of convection-driven dynamos in rotating spherical shells and application to planetary magnetic fields, *Geophys. J. Int.*, *166*, 97–114.

Chulliat, A., and K. Telali (2007), World monthly means database project, *Publ. Inst. Geophys. Pol. Acad. Sci.*, *C-99*(398), 537–552.

Constable, C. G., R. L. Parker, and P. N. Stark (1993), Geomagnetic field models incorporating frozen-flux constraints, *Geophys. J. Int.*, *113*, 419–433.

Eymin, C., and G. Hulot (2005), On core surface flows inferred from satellite magnetic data, *Phys. Earth Planet. Inter.*, *152*, 200–220.

Fournier, A., C. Eymin, and T. Alboussière (2007), A case for variational geomagnetic data assimilation: Insights from a one-dimensional, nonlinear and sparsely observed MHD system, *Nonlinear Processes Geophys.*, *14*, 1–18.

Ghil, M. (1997), Advances in sequential estimation for atmospheric and oceanic flows, *J. Meteorol. Soc. Jpn.*, *75*, 289–304.

Ghil, M., et al. (2002), Advanced spectral methods for climatic time series, *Rev. Geophys.*, *40*(1), 1003, doi:10.1029/2000RG000092.

Gubbins, D. (1983), Geomagnetic field analysis—I. Stochastic inversion, *Geophys. J. R. Astron. Soc.*, *73*, 641–652.

Gubbins, D. (2007), Geomagnetic constraint on stratification at the top of the core, *Earth Planets Space*, *59*, 661–664.

Gubbins, D., and J. Bloxham (1985), Geomagnetic field analysis—II. Magnetic fields on the core-mantle boundary, *Geophys. J. R. Astron. Soc.*, *80*, 695–713.

Hills, R. G. (1979), Convection in the Earth's mantle due to viscous shear at the core-mantle interface and due to large-scale buoyancy, Ph.D. thesis, N. M. State Univ., Las Cruces.

Holme, R. (2007), Large scale flow in the core, in *Treatise on Geophysics*, vol. 8, *Core Dynamics*, pp. 107–129, edited by P. Olson and G. Schubert, Elsevier, Amsterdam.

Holme, R., and N. Olsen (2006), Core surface flow modelling from high-resolution secular variation, *Geophys. J. Int.*, *166*, 518–528.

Hongre, L., G. Hulot, and A. Khokhlov (1998), An analysis of the geomagnetic field over the past 2000 years, *Phys. Earth Planet. Inter.*, *106*, 311–335.

Hulot, G., and J.-L. Le Mouël (1994), A statistical approach to the Earth's main magnetic field, *Phys. Earth Planet. Int.*, *82*, 167–183.

Hulot, G., J.-L. Le Mouël, and J. Wahr (1992), Taking into account truncation problems and geomagnetic model accuracy in assessing computed flows at the core-mantle boundary, *Geophys. J. Int.*, *108*, 224–246.

Hulot, G., N. Olsen, and T. J. Sabaka (2007), The present field, in *Treatise on Geophysics*, vol. 5, *Geomagnetism*, pp. 33–75, edited by M. Kono and G. Schubert, Elsevier, Amsterdam.

Jackson, A. (1997), Time-dependency of tangentially geostrophic core surface motions, *Phys. Earth Planet. Inter.*, *103*, 293–311.

Jackson, A., J. Bloxham, and D. Gubbins (1993), Time-dependent flow at the core surface and conservation of angular momentum in the coupled core-mantle system, in *Dynamics of the Earth's Deep Interior and Earth Rotation*, *Geophys. Monogr. Ser.*, vol. 72, edited by J.-L. Le Mouël, D. E. Smylie, and T. Herring, pp. 97–107, AGU, Washington, D. C.

Jackson, A., C. G. Constable, M. R. Walker, and R. L. Parker (2007), Models of Earth's main magnetic field incorporating flux and radial vorticity constraints, *Geophys. J. Int.*, *171*, 133–144.

Jault, D. (2008), Axial invariance of rapidly varying diffusionless motions in the Earth's core interior, *Phys. Earth Planet. Inter.*, *166*, 67–76.

Jault, D., C. Gire, and J. Le Mouël (1988), Westward drift, core motions and exchanges of angular momentum between core and mantle, *Nature*, *333*, 353–356.

Kalnay, E. (2003), *Atmospheric Modeling, Data Assimilation and Predictability*, Cambridge Univ. Press, Cambridge, U. K.

Lancaster, P., and K. Salkauskas (1986), *Curve and Surface Fitting: An Introduction*, Academic, New York.

Lehnert, B. (1954), Magnetohydrodynamic waves under the action of the Coriolis force, *Astrophys. J.*, *119*, 647–654.

Le Mouël, J.-L. (1984), Outer core geostrophic flow and secular variation of Earth's geomagnetic field, *Nature*, *311*, 734–735.

Le Mouël, J.-L., C. Gire, and T. Madden (1985), Motions of the core surface in the geostrophic approximation, *Phys. Earth Planet. Inter.*, *39*, 270–287.

Lesur, V., I. Wardinski, M. Rother, and M. Mandea (2008), GRIMM: The GFZ Reference Internal Magnetic Model based on vector satellite and observatory data, *Geophys. J. Int.*, *173*, 382–394.

Madden, T., and J.-L. Le Mouël (1982), The recent secular variations and the motions at the core surface, *Philos. Trans. R. Soc. London*, *306*, 271–280.

O'Brien, M. S., C. G. Constable, and R. L. Parker (1998), Frozen flux modelling for epochs 1915 and 1980, *Geophys. J. Int.*, *128*, 434–450.

Olsen, N., and M. Mandea (2007), Investigation of a secular variation impulse using satellite data: The 2003 geomagnetic jerk, *Earth Planet. Sci. Lett.*, *255*, 94–105.

Olsen, N., and M. Mandea (2008), Rapidly changing flows in the Earth's core, *Nat. Geosci.*, *1*, 390–394.

Olsen, N., H. Luhr, T. J. Sabaka, and M. Mandea (2006), CHAOS—A model of Earth's magnetic field derived from CHAMP, Oersted, and SAC-C magnetic satellite data, *Geophys. J. Int.*, *166*, 67–75.

Pais, M. A., and G. Hulot (2000), Length of the day decade variations, torsional oscillations and inner core super-rotation: Evidence from recovered core surface zonal flows, *Phys. Earth Planet. Inter.*, *118*, 291–316.

Pais, M. A., and D. Jault (2008), Quasi-geostrophic flows responsible for the secular variation of the Earth's magnetic field, *Geophys. J. Int.*, *173*, 421–443.

Pais, M. A., O. Oliveira, and F. Nogueira (2004), Nonuniqueness of inverted core-mantle boundary flows and deviation from tangential geostrophy, *J. Geophys. Res.*, *109*, B08105, doi:10.1029/2004JB003012.

Renka, R. J. (1997), Algorithm 772: Delaunay Triangulation and Voronoi diagram on the surface of a sphere, *Trans. Math. Software*, *23*, 416–434.

Sabaka, T. J., N. Olsen, and M. E. Purucker (2004), Extending comprehensive models of the Earth's magnetic field with Oersted and CHAMP data, *Geophys. J. Int.*, *159*, 521–547.

Starchenko, S. V., and C. A. Jones (2002), Typical velocities and magnetic field strengths in planetary interiors, *Icarus*, *157*, 426–435.

Talagrand, O. (1997), Assimilation of observations, an introduction, *J. Meteorol. Soc. Jpn.*, *75*, 191–209.

Talagrand, O., and P. Courtier (1987), Variational assimilation of meteorological observations with the adjoint vorticity equation. I: Theory, *Q. J. R. Meteorol. Soc.*, *113*, 1311–1328.

Turner, G. M., J. L. Rasson, and C. V. Reeves (2007), Observation and measurement techniques, in *Treatise on Geophysics*, vol. 5, *Geomagnetism*, pp. 93–146, edited by M. Kono and G. Schubert, Elsevier, Amsterdam.

Waddington, R., D. Gubbins, and N. Barber (1995), Geomagnetic field analysis—V. Determining steady core surface flows directly from geomagnetic observations, *Geophys. J. Int.*, *122*, 326–350.

Wardinski, I. (2004), Core surface flow models from decadal and subdecadal secular variation of the main geomagnetic field, Ph.D. thesis, Freie Univ., Berlin.

Wardinski, I., and R. Holme (2006), A time-dependent model of the Earth's magnetic field and its secular variation for the period 1980–2000, *J. Geophys. Res.*, *111*, B12101, doi:10.1029/2006JB004401.

Wunsch, C. (2000), *Discrete Inverse and State Estimation Problems*, Cambridge Univ. Press, Cambridge, U. K.

Zatman, S., and J. Bloxham (1997), Torsional oscillations and the magnetic field within the Earth's core, *Nature*, *388*, 760–763.